Correction date: 22 December, 2022

The Obscuring Effect of Magma Recharge on the Connection of Volcanic-Plutonic Rocks

Kai Zhao[1], Xisheng Xu[1]*, Zhenyu He[2], and Yan Xia[1]

[1]State Key Laboratory for Mineral Deposits Research, School of Earth Sciences and Engineering, Nanjing University, Nanjing, 210023, China;

[2]School of Civil and Resource Engineering, University of Science and Technology Beijing, Beijing 100083, China;

*Corresponding author: Xisheng Xu (xsxu@nju.edu.cn)

Abstract

The current debate on volcanic-plutonic connection is centered on whether efficient liquid-crystal segregation dominates the evolution of a mushy reservoir to produce evolved, crystal-poor rhyolite and cumulate leftover. However, magma recharge may remarkably influence the evolution of a mushy reservoir and obscure the evidence of liquid-crystal segregation. This complexity poses a challenge to exploring the connection of volcanic-plutonic rocks. This study investigates the Qinzhou Bay granitic complex (~250-248 Ma) from South China, which contains crystal-poor (<19 vol%) peraluminous rhyolites and subsequent crystal-rich (28-54 vol%) porphyries. Although the rhyolite and porphyry units have a close spatio-temporal link, they do not share a fractionation trend and similar whole-rock Sr-Nd-O isotopic compositions; thus, a direct connection is not evidenced. We further present textural analyses, mineral and melt inclusion compositions, thermobarometry (the combination of Ti-in-zircon thermometer and Ti-in-quartz thermobarometer), and thermodynamic modeling to examine the alternative interpretations, i.e., the two units have intrinsically independent origins or the connection of the two units has been obscured. For the rhyolite unit, thermobarometric results reveal a polybaric storage system consisting of middle (>600±80 MPa) and upper (~150±40 MPa and ~60±20 MPa) crustal reservoirs. Variations in quartz Fe content and chlorine-rich, metaluminous melt inclusions suggest that magma hybridization with less-evolved metaluminous magmas occurred at both crustal levels. In particular, the elevated Fe contents in the quartz population that crystallizes at the shallowest level (~60±20 MPa) suggest that recharge magmas were directly injected into the shallowest reservoir. Deviation of the whole-rock composition from the liquid evolution trend recorded in melt inclusions suggests a combined effect of magma mixing and crystal-melt segregation processes in upper crustal reservoirs. Thermodynamic modeling and

mass balance calculations suggest that the whole-rock composition of the rhyolite could be reproduced by mixing between regionally exposed dacites and segregated melts at crystallinities of 50-60% (the parental magma represented by the least evolved melt inclusion). For the porphyry unit, thermobarometric results reveal magma storage at middle (more than 450±40 MPa to 550±40 MPa) and upper (110±20 MPa to 140±20 MPa) crustal levels. The small-scale oscillatory zonation of plagioclase, the pervasive resorption of quartz and alkali feldspar, and the presence of peraluminous microgranular enclaves in the porphyries suggest a recharge event of metasediment-sourced magmas, triggering reactivation and convection of the reservoir. Autoclastic and overgrowth textures of quartz, plagioclase, and alkali feldspar phenocrysts and development of columnar jointing suggest that the reactivated porphyritic magmas ascended and emplaced at ultrashallow levels (~30±10 MPa).

Because of the similar storage pressures, the porphyries may represent remobilized cumulates of rhyolitic magmas, whereas the texture and geochemistry of the cumulate-liquid pair were modified, a key factor rendering a cryptic connection between the rhyolite and porphyry. Alternatively, the plumbing systems feeding the rhyolite and porphyry units are horizontally independent or vertically discrete, but this circumstance is inconsistent with the same evolution trend of quartz Fe and Al contents of the rhyolite and porphyry. Our study highlights that whole-rock composition may record blended information of complex processes, and caution should be taken when whole-rock composition is used to extract information of a single process. Multidisciplinary constraints are required to evaluate the influence of recharge processes on the modification of liquid-cumulate records, and big data analysis on the basis of geochemistry should be conducted with caution to avoid biased understanding.

Keywords: Liquid-crystal segregation; magma recharge; peraluminous rhyolite; porphyry; thermodynamic modeling

Introduction

Deciphering the connection of silicic volcanic and plutonic rocks is critical to understand the formation of high-silica rhyolites and the differentiation of continental crust (e.g., Bachmann et al. 2007; Keller et al. 2015; Deering et al. 2016; Watts et al. 2016; Karakas et al. 2019; Tavazzani et al. 2020). The crystal mush extraction model suggests that crystal-poor rhyolite tightly connects with the underlying mushy reservoir through a liquid-crystal segregation process (Bachmann and Bergantz 2004; Hartung et al. 2017; Holness 2018; Schaen et al. 2018). This model has been supported by a number of studies on caldera complexes where coexisting volcanic and plutonic rocks generally crystallize simultaneously and have complementary liquid-cumulate geochemistry (e.g., Deering et al. 2016; Yan et al. 2016, 2018; Xu et al. 2021). In contrast, big data analyses of global volcanic and plutonic rocks reveal little evidence for significant segregation of liquid from plutons (Keller et al. 2015).

The discrepancy may simply imply that liquid-crystal segregation in mushy reservoirs does not appear to be a volumetrically significant mechanism for the production of silicic volcanic rocks (Keller et al. 2015). Alternatively, another possibility is related to the effect of magma recharge on the evolution of mushy reservoirs. Magma recharge may reactivate the rheologically locked crystal mush, and the subsequent convective stirring and rehomogenization of the mushy reservoirs could eliminate the compositional gradient established by liquid-crystal segregation (Hildreth 1981; Bachmann and Bergantz 2006; Huber et al. 2010, 2012). Moreover, magma mixing during recharge has long been considered one of the major causes of magma diversity (e.g., Morgavi et al. 2022). The recharge magmas may have diverse compositions varying from mafic (Eichelberger et al. 2006; Ruprecht et al. 2012) to silicic (Eichelberger et al. 2000; Shaw and Flood 2009; Chamberlain et al. 2015; Watts et al. 2016). Therefore, the consequent hypothesis is that multiple episodes of recharge events may obscure the evidence of crystal-liquid segregation in a mushy reservoir and thus render a cryptic connection of volcanic and plutonic units.

The hypothesis could be tested by investigations on peraluminous rhyolites (with the presence of normative corundum). Previous studies on the isotope geochemistry of the paired volcanic-plutonic rocks reveal instructive results, i.e., metaluminous volcanics and their plutonic counterparts share similar isotopic compositions, yet peraluminous volcanic-granitic rocks record different isotopic compositions (Kemp et al. 2008). The latter suggests that peraluminous rhyolites may be not linked to coexisting plutonic rocks or that their linkage has been disrupted by open-system processes (e.g., mixing or assimilation, as suggested by Kemp et al. 2008). Exploring these alternative interpretations thus requires examining the mineral-scale records and exploring the involved magmatic processes.

In this study, we investigate a peraluminous complex from Qinzhou Bay, South China, which exhumes volcanic rocks (rhyolitic lava and tuff), subvolcanic porphyries, and coarse-grained granite plutons by a series of post-magmatic thrust faults (Fig. 1a, b). The coarse-grained granites have been suggested to form a zoned pluton that records compaction-driven liquid-crystal segregation, as evidenced by the microtexture and microstructure features (Zhao et al. 2018), whereas the available whole-rock element and isotope geochemistry precludes a direct derivation of the rhyolite from the granitic plutons (Qin et al. 2011; Jiao et al. 2015). Integrating the published whole-rock data for this complex, we further present field observations, mineral textures and compositions, whole-rock and melt inclusion compositions, and thermobarometry to explore the magmatic processes involved in the formation of the rhyolites and porphyries. The aim of this study is to evaluate whether these units are intrinsically independent, or alternatively, if open-system processes obscure the liquid-cumulate records.

Geological backgrounds

The Qinzhou Bay Granitic Complex (QBGC), bounded by several NE-trending thrust faults, consists of volcanic rocks of the Banba Formation, Taima and Dasi porphyries, and Jiuzhou granite pluton (Fig. 1a, b). Secondary ion mass spectroscopy (SIMS) zircon U–Pb dating for these units yielded roughly contemporary ages within analytical errors (248±1.6 Ma to 250±1.7 Ma, Qin et al. 2011; Jiao et al. 2015). The granitic plutons intruded Paleozoic rocks such as metasedimentary rocks (gneiss, schist, quartzite, and marble) and sedimentary rocks (shale and limestone; Fig. 1b; Zhao et al. 2017b). These country rocks are also present as abundant metasedimentary enclaves in the granitic plutons. Two types of restitic granulite enclaves have been identified in the granitic plutons, i.e., orthopyroxene- and plagioclase-rich enclaves in the Taima and Dasi porphyries record melting conditions of ~950 ± 30 °C and ~500 ± 80 MPa, while garnet-rich and plagioclase-poor enclaves in the Jiuzhou pluton record higher pressures of ~675 ± 25 MPa and slightly lower temperatures of ~905 ± 15 °C (Jiao et al. 2013; Zhao et al. 2017b). Crystal aggregates consisting of orthopyroxene-plagioclase-ilmenite (Opx-Pl-Ilm) are present in the Taima and Dasi porphyries. The mineral assemblage and texture of the crystal aggregates are similar to those of the hosted granulite enclaves. These crystal aggregates have been considered to be microscale fragments of granulite enclaves, thus representing restitic materials (Zhao et al. 2017b). The tectonic setting where these rocks formed has long been considered to be related to collision between the South China and Indochina blocks (e.g., Zhou et al. 2006), but subduction of the Paleo-Tethys (Hu et al. 2015) or Paleo-Pacific (Jiao et al. 2015) oceanic plate has also been proposed as an alternative.

Samples and methods

Sample preparation

Imaging and analyses of minerals were conducted in thin sections for ~30 fresh samples of the volcanic and plutonic rocks and for 3 samples of xenolith (one gneiss and two schist samples hosted by the Dasi porphyry and the Jiuzhou pluton). Quartz and zircon from ~10 samples of the rhyolitic lavas and porphyritic rocks were also prepared by standard heavy liquid and magnetic separation methods. Representative grains (>200 grains for each sample) were then mounted in epoxy resin. Completely crystallized melt inclusions hosted in quartz phenocrysts of the Banba rhyolite were homogenized in eight doubly polished thin sections, and quartz phenocrysts containing melt inclusions were also picked out and mounted in epoxy resin after homogenization (see details in supplementary file). Homogenization techniques followed the protocol of Student and Bodnar (1999, 2004).

Geochemical analyses for minerals, melt inclusions, and groundmasses

Major elements of plagioclase, alkali feldspar, and melt inclusions were acquired using a JEOL JXA-8230 electron microprobe at the State Key Laboratory for Mineral Deposits Research (LAMD), Nanjing University (see supplementary file). For analyses of minerals, we used a beam size of 1-5 μm, an accelerating potential voltage of 15 kV, and a probe current of 15 nA. For analyses of melt inclusions, we used a probe current of 2-4 nA and a defocused beam size of 5-15 μm to minimize the problem of Na loss. Before analyses of zircon and quartz trace elements, cathodoluminescence (CL), transmitted and reflected images were obtained for selecting mineral domains to avoid mineral inclusions and fractures. Quartz and zircon trace elements were then analyzed with laser ablation inductively coupled plasma–mass spectrometry (LA-ICP–MS) at LAMD. Analyses were conducted on polished thin sections (>100 μm thick) and epoxy mounts using a Thermo-Finnigan Element 2 sector field ICP–MS coupled with a 193 nm ArF Excimer laser (GeoLasPro system, Coherent, USA). Analytical uncertainties for quartz and zircon trace elements are usually better than 5% and 10% (1σ, see supplementary Table S1), respectively. The quality of zircon analyses was appraised based on the compositional indices of La contents and LREE-I (=Dy/Sm + Dy/Nd), and appropriate analyses should yield <0.32 ppm (parts per million) La and >30-60 LREE-I (Burnham 2020). Major elements of completely crystalline groundmass were analyzed using a Micro X-ray fluorescence spectrometer at LAMD (see supplementary file). The analyses typically cover areas larger than 500 μm × 500 μm and depths <100 μm and may include small autoclastic fragments of phenocrysts and tiny crystals (e.g., ilmenite) that should belong to phenocryst assemblages. The compositional data will be used to evaluate the homogeneity of the groundmass.

Whole-rock geochemical analyses

Whole-rock data of major and trace elements and Sr-Nd isotopes for the Taima and Dasi porphyries (12 samples) and the Jiuzhou pluton (7 samples) have been published in Zhao et al. (2017b). In this study, new whole-rock analyses of major and trace elements and Sr-Nd isotopes were conducted for the Banba rhyolitic lavas (3 samples) and the Jiuzhou pluton (2 samples) at LAMD, Nanjing University (see detailed methods in the supplementary file). These whole-rock data are combined with published whole-rock data for the Banba rhyolitic lavas (12 samples; Qin et al. 2011; Jiao et al. 2015) to capture the main compositional variation in the QBGC. In addition, oxygen isotope analyses (see methods in supplementary file) for seven samples from the Banba rhyolite and the Taima and Dasi porphyries were conducted in the ALS Minerals Laboratory, Guangzhou, China, together with published zircon oxygen isotope data (Jiao et al. 2015), to evaluate the influence of hydrothermal alteration on volcanic and subvolcanic rocks.

Thermodynamic modeling

Thermodynamic modeling affords a powerful tool to constrain the phase relationship of magma crystallization (e.g., Rhyolite_MELTS, Gualda et al. 2012a; Perple_X, Connolly, 2005). The Perple_X software package is mostly used in this study because it has been successful in reproducing the phase relationship of peraluminous magma systems at relatively low pressure (≤200 MPa) and H_2O-poor (≤2 wt% H_2O total) conditions (e.g., Clemens et al. 2014; Zhao et al. 2017a; Wu et al. 2018). This method yields comparable results to experiment-based phase relationships within uncertainties of 20-60 °C, especially quartz saturation temperatures within an uncertainty of 20 °C (Zhao et al. 2017a). Rhyolite_MELTS software is also employed to fit the compositional evolution of the more hydrous, metaluminous melt inclusions (see below).

Diffusion modeling

Intracrystalline diffusion of Ti in zoned quartz for the Banba rhyolite was modeled using the standard diffusion equation (e.g., Gualda et al. 2012b; Tavazzani et al. 2020) and experimentally calibrated diffusivity of Ti in quartz (Audétat et al. 2021). The modeling likely has uncertainties of 217-240% on the diffusive relaxation time, which incorporate uncertainties related to the diffusion coefficient (18-22%), temperature (42-50%), and curve fitting of quartz Ti profiles

(150-180%, Gualda et al. 2012b; Wu et al. 2022). Modeling results are provided in supplementary table S3, and more details of governing equations, numerical solution, selection of diffusivity, and uncertainty analyses are provided in the supplementary file.

Field observation and petrography

Banba rhyolite

The volcanic rocks of the Banba Formation are dominated by rhyolitic rocks, including effusive lava and minor tuff. The tuff layers, consisting of accretionary lapilli tuff and crystal welded tuff (Fig. 1c), conformably overlie sedimentary strata (e.g., limestone; Fig. 1c). The rhyolitic lavas extend for ~50 km along a NE-striking fault system (Fig. 1b). The lavas are gray–green in hand specimens with the development of magma flow structures. The phenocryst (<19 vol%) assemblage consists of quartz (<6 vol%), plagioclase (<9 vol%), cordierite (<3 vol%), and orthopyroxene (<1 vol%). No alkali feldspar phenocrysts are present in our samples. A small number of xenolithic/xenocrystic materials with round shapes and dark brown colors are present in individual samples (BB02-1; Supplementary Fig. S1a).

Quartz phenocrysts with grain sizes of 0.5-2 mm are significantly resorbed with round or embayed crystal outlines (Fig. 2a, b). They are largely unzoned in CL-based imaging (Fig. 2c), whereas a proportion of quartz phenocrysts develop inverse zonation with a lighter gray rim and a darker core (Fig. 2d). The quartz phenocrysts occasionally contain melt inclusions, which occur as isolated individuals or small groups (Fig. 2d). These melt inclusions are completely crystallized and contain distorted vapor bubbles that fill the interstices between the daughter crystals and the host walls. After homogenization, melt inclusions are largely homogeneous (Fig.

2d), but some of them may contain minor (<5 vol%) unmelted opaque minerals (e.g., iron oxides).

Plagioclase phenocrysts with grain sizes of 0.5-3 mm have round or embayed outlines, showing resorption features (Fig. 2a). Zonation of plagioclase has not been observed due to alteration, such as saussuritization and carbonatization (Supplementary Fig. S1b). Orthopyroxene crystals are rarely present with anhedral shapes due to alteration. Cordierite crystals with sizes of <1 mm have elongated to round shapes and partially developed crystal surfaces with rare mineral inclusions (Fig. S1c) and have been partly altered to chlorite. The groundmass of the rhyolite consists of elongated dendritic quartz, interstitial alkali feldspar with grain sizes of ~10-100 μm (Fig. 2b), and accessory minerals such as zircon, titanite and ilmenite.

Taima and Dasi porphyries

The Taima and Dasi porphyritic rocks form an elliptical composite cryptodome covering an area of ~1200 km^2 bounded by a set of ring-radial faults (Fig. 1b). The Taima porphyry is observed to locally extrude and overlie the accretionary lapilli tuff and crystal welded tuff layers (Fig. 1c). Columnar jointing is also observed at the roof of the Taima porphyritic cryptodome (Fig. 3a). The two porphyritic bodies share similar textures and mineral assemblages, consisting of alkali feldspar, quartz, plagioclase, cordierite, orthopyroxene and biotite. Compared with the Taima porphyritic rocks, the Dasi rocks have higher contents of phenocrysts (48-54 vol% versus 29-45 vol%) and a coarser groundmass (<200 μm versus <50-100 μm). The groundmass of both porphyritic rocks consists of quartz, alkali feldspar, minor plagioclase, biotite, and accessory minerals such as zircon and ilmenite. The quartz in the groundmass has subhedral forms with partially developed hexagonal crystal faces (Fig. 3b), a feature that is different from the elongated, dendritic quartz in the groundmass of the Banba rhyolite (Fig. 2b).

Quartz phenocrysts with a maximum size of up to ~6 mm have round or embayed crystal outlines (Fig. 3c, d). These resorbed quartz phenocrysts were broken into several angular fragments, and sometimes these fragments remained together (Fig. 3c). This autoclastic texture is common in the Taima porphyry but not apparent in the Dasi porphyry (Fig. 3d). The quartz phenocrysts in the Taima and Dasi porphyries develop bright and thin (~10-50 μm) overgrowths surrounding a darker core in CL-based imaging (Fig. 3e, f). The quartz overgrowth is characterized by a poikilitic texture where the included crystals are alkali feldspar (Fig. 3e, f).

Plagioclase phenocrysts with sizes of 0.2-2 mm seldom have round or embayed crystal outlines but mostly occur as tabular crystals (Fig. 3c, d) or angular fragments. Alkali feldspar phenocrysts with sizes of up to ~3 mm in the Taima and Dasi porphyries have embayed crystal outlines (Fig. 3c, d). Biotite crystals are rarely (<0.4 vol%) present as both phenocrysts and groundmass minerals. Cordierite crystals with euhedral shapes and 0.2-1 mm sizes have been altered to chlorite or serpentine. Orthopyroxene phenocrysts are present as euhedral to subhedral crystals with grain sizes of 0.5-2.2 mm (mostly 0.8-1.5 mm).

Jiuzhou pluton

The Jiuzhou composite pluton includes two phases: the early phase consists of gray–white orthopyroxene-free monzogranites, while the predominant late phase consists of gray–black, orthopyroxene-bearing granodiorite (i.e., charnockite) at low elevations that gradually zoned to relatively evolved orthopyroxene-free monzogranite at high elevations. A clear intrusive relationship between the two phases is observed in the field, where the late unit has a chilled

DOI: https://doi.org/10.2138/am-2022-8642. http://www.minsocam.org/

margin (with finer grains and darker color) at the contact boundary and contains blocks of the early Jiuzhou monzogranite (Fig. S2). More detailed descriptions of petrography are provided in the supplementary file (Text S8) and can be found in Zhao et al. (2018).

Analytical results

Mineral composition and zonation

Quartz. Quartz Ti contents in the rhyolite and porphyry units vary from ~50 ppm to ~350 ppm, and they are roughly clustered into three groups, as revealed by the probability density distributions, i.e., Group A with 323±36 ppm (2σ, two standard deviations), Group B with 204±54 ppm, and Group C with 101±48 ppm (Fig. 4a). Group A crystals are dominantly present in the Banba rhyolite and occur as single crystals (Fig. 2c) or bright rims of Groups B and C crystals (Fig. 2d; Fig. 5). In the Taima and Dasi porphyry, the bright and thin (10-50 μm) overgrowths of quartz crystals have high Ti contents (up to ~330-350 ppm, inferred from Cl intensity, Fig. 5c, d) that are equal to the Ti contents of the Group A crystals in the Banba rhyolite. Groups B and C crystals are dominantly present in the Taima and Dasi porphyries but are also included in the Banba rhyolite (Fig. 4a, b). Group A crystals in the Banba rhyolite have 365-660 ppm Al and 100-200 ppm Fe, which are higher than 290-580 ppm Al and <100 ppm Fe for other groups of crystals (Fig. 4a, b). The Groups B and C crystals from the rhyolite and porphyry have similar Al (300-500) and Fe contents (50-100 ppm).

Quartz crystals from both the Jiuzhou pluton and the country rock xenoliths are analyzed for comparison. Quartz crystals in the late Jiuzhou charnockites have similar Ti and Al contents (Fig. 4a) but systematically lower Fe contents (<50 ppm; Fig. 4b) compared to Groups B and C crystals in the rhyolite and porphyry units. Quartz crystals in the early Jiuzhou monzogranites have Ti contents comparable to those of Group C quartz, but Al (<300 ppm) and Fe (<60 ppm) contents of the early Jiuzhou quartz are systematically lower than those of Group C quartz (Fig. 4a, b). Quartz crystals in the xenoliths have Ti contents comparable to those of Groups B and C quartz in the rhyolite and porphyry units, but quartz Al (<350 ppm) and Fe (<60 ppm) contents in the xenoliths are approximate to those in the early and late Jiuzhou granites (Fig. 4a, b). On the Fe versus Al diagram (Fig. 4c), the same variation trend is defined by part of Group A quartz in the rhyolite unit, Groups B and C quartz in the rhyolite and porphyry units, and quartz in the early Jiuzhou monzogranites, while quartz crystals in the late Jiuzhou charnockites have a different variation trend from those in other units.

Plagioclase. In the Banba rhyolite, the plagioclase phenocrysts have high albite contents (~Ab_{86-95}), but these data are not representative of primary magmatic composition due to alteration. In the Taima and Dasi porphyries, the plagioclase phenocrysts have similar compositions and zonations. They have high-anorthite cores with an average composition of ~An_{50} and narrow (~10 μm) overgrowths with an average composition of ~An_{35} (~An_{32-42}, Fig. 6; Fig. 7a, b). The majority of the plagioclase cores are largely unzoned or weakly zoned, while some (<20%) plagioclase crystals have oscillatory zonation characterized by resorption surfaces at 5-10 μm (Fig. 6a) or 40-50 μm (Fig. 6b-c) spacing and by compositional fluctuations at scales of ~An_{5-7} (Fig. 6d-f). The groundmass plagioclase crystals have a similar composition (~An_{23-38}) to the overgrowth of phenocrysts (Fig. 7c).

Alkali feldspar. The alkali feldspar phenocrysts in the Taima and Dasi porphyries have low-orthoclase cores with an average composition of ~Or_{71} and narrow (50-100 μm) overgrowths with higher orthoclase contents (up to ~Or_{82}; Supplementary dataset S1). The alkali feldspar crystals in the groundmass have compositions of Or_{72-77}, which are slightly higher than those of the phenocryst cores (Supplementary dataset S1).

Zircon. Compared to zircon crystals from the Taima and Dasi porphyries and the Jiuzhou charnockites, zircon crystals from the Banba rhyolites have slightly higher Ti contents (10-26 ppm versus 6-21 ppm; Fig. 8a), lower P contents (160-880 ppm versus 400-1300 ppm; Fig. 8b), and higher values of Eu/Eu* (0.02-0.07 versus <0.04; Fig. 8a), Nb/Ta (1.3-2.6 versus 0.8-2.1; Fig. 8c) and Zr/Hf (44-81 versus 40-70; Fig. 8d), although compositional distributions partly overlap among these units. The outliers with high Eu/Eu* ratios of 0.12-0.17 are not considered here because they may not represent autocrysts that crystallized from the magmas (Fig. 8; see below). Zircon crystals in the Banba rhyolite have relatively bright rims surrounding darker cores in CL images (Fig. S3a; excluding those crystals with inherited/xenocrystic cores, Supplementary dataset S1), but the core-rim Ti compositions show small differences, i.e., on average 15.2±2.0 ppm versus 12.7±1.9 ppm for the rims and cores, respectively (Supplementary dataset S1). For the Taima and Dasi porphyries, compositional differences between zircon cores and rims are indistinguishable in both CL intensities (Fig. S3b) and Ti contents (on average, 11.6±1.8 ppm and 12.1±1.6 ppm for rims and cores, respectively).

Melt inclusions and whole-rock compositions

Melt inclusions in the Banba rhyolite have a wide range of compositions with SiO_2 contents from ~70 wt% to ~76 wt%, which cover the range of whole-rock compositions with ~70 wt% to ~72 wt% SiO_2 (Fig. 9). These inclusions are mostly present in the Group B quartz crystals but rarely in other groups (one in Group A quartz; Supplementary dataset S2). The melt inclusion and whole-rock compositions do not share the same fractionation trend. The whole-rock composition has systematically lower Al_2O_3 (by <2.75 wt%, Fig. 9a), Na_2O (by <3 wt%, Fig. 9e) and K_2O (by <3 wt%, Fig. 9f) contents but higher Fe_2O_3 (by <4 wt%, Fig. 9b), MgO (by <1 wt%, Fig. 9c) and CaO (by <2 wt%, Fig. 9d) contents at the same SiO_2 content. Another notable feature is that the melt inclusions overall have metaluminous compositions (A/CNK values mostly at 0.82-0.98 with two exceptions at 1.04 and 1.10), but the whole-rock compositions are weakly to strongly peraluminous (A/CNK values mostly at 1.01-1.14; Supplementary dataset S2). The volatile species in melt inclusions are dominated by Cl (190-2050 ppm) with minor detectable F (<320 ppm, supplementary dataset S2). The groundmasses of the Banba rhyolite with limited variations in compositions (with ~75 wt% SiO_2 contents) are more evolved than the whole-rock compositions (Fig. 9). Compared with the melt inclusions, the groundmasses have higher Fe_2O_3 (by ~1 wt%, Fig. 9b) and K_2O (by ~1 wt%, Fig. 9f) contents but lower Na_2O (by ~1.2 wt%, Fig. 9e) contents with comparable SiO_2 contents.

The Taima and Dasi porphyries have whole-rock SiO_2 contents of 68 wt% to 74 wt%, overlapping with those exhibited by the rhyolites (Fig. 9a-f; Zhao et al. 2017b). The groundmasses of the porphyries with SiO_2 contents of 74-77 wt% are more evolved than the whole-rock compositions. The Taima and Dasi porphyries do not share a consistent variation trend with the rhyolites, e.g., the porphyry samples have clearly higher whole-rock Al_2O_3 and CaO contents (Fig. 9a, c) but lower whole-rock Fe_2O_3 contents (Fig. 9b) than the bulk rhyolite samples. The early Jiuzhou monzogranites have whole-rock compositions similar to those of the Taima and Dasi porphyries. The late Jiuzhou pluton shares a similar variation trend with the volcanic rocks in the whole-rock Al_2O_3, Fe_2O_3, Na_2O and K_2O versus SiO_2 diagrams (Fig. 9a, b, e, f) but not in the whole-rock MgO and CaO versus SiO_2 diagrams (Fig. 9c, d).

DOI: https://doi.org/10.2138/am-2022-8642. http://www.minsocam.org/

Whole-rock isotopic geochemistry

The studied volcanic and plutonic rocks have distinguishable differences in whole-rock Sr-Nd-O isotope compositions, and all rocks have an isotopic signature of reworked crust. The Banba rhyolites have apparently lower initial $^{87}Sr/^{86}Sr$ ratios (<0.71828 versus 0.7190-0.7217) and higher initial $^{143}Nd/^{144}Nd$ ratios (0.51178-0.51181 versus 0.51172-0.51177) than the Taima and Dasi porphyries and the early and late Jiuzhou granites (Fig. 10a; Supplementary dataset S2). The Banba tuff samples have Nd isotope compositions (initial $^{143}Nd/^{144}Nd$ ratios of 0.51180-0.51181) similar to those of the rhyolite samples (Supplementary dataset S2). For whole-rock oxygen isotopes, the Banba rhyolites have slightly lower $\delta^{18}O$ values than the Taima and Dasi porphyries (9.4-10.6 ‰ versus 11.1-12.4 ‰, respectively; with 2σ error of 0.3 ‰; Fig. 10b).

Constraints on P–T conditions

Estimation of magmatic P–T conditions is critical to characterize magma plumbing systems and their evolution but remains challenging (especially for pressure; e.g., Blundy and Cashmann, 2008; Erdmann et al. 2019). Ti-in-quartz thermobarometry (Thomas et al. 2010; Huang et al. 2012; Zhang et al. 2020; Osborne et al. 2022) potentially provides constraints on P–T conditions only when one of the P–T parameters is known. Ti-in-zircon thermometry (Ferry and Watson, 2007; Loucks et al. 2020) has been widely used to estimate crystallization temperature. Therefore, a possible approach is to combine Ti-in-quartz thermobarometry and Ti-in-zircon thermometry if quartz and zircon crystallize simultaneously or the relative sequence of crystallization for the two phases is constrained. Thermodynamic modeling can provide independent constraints on the phase relationship and thus crystallization sequence. In the following, the feasibility of the approach is tested for the QBGC.

This is the peer-reviewed, final accepted version for American Mineralogist, published by the Mineralogical Society of America.
The published version is subject to change. Cite as Authors (Year) Title. American Mineralogist, in press.
DOI: https://doi.org/10.2138/am-2022-8642. http://www.minsocam.org/

Ti-in-zircon thermometry

The calibration of the Ti-in-zircon thermometer by Ferry and Watson (2007) incorporated the effects of TiO_2 and SiO_2 activities, and Loucks et al. (2020) recently proposed a revised Ti-in-zircon thermometer incorporating the effect of pressure. Our evaluation suggests that the former thermometer is reasonably consistent with the previous estimations from the two-feldspar thermometer and constraints from thermodynamic modeling for the QBGC rocks (Zhao et al. 2017a), while the latter yields unrealistically high median temperatures of >900 °C at pressures of <500 MPa (Fig. S4). We thus use the Ti-in-zircon thermometer by Ferry and Watson (2007) in this study.

The activity of TiO_2 ($aTiO_2$) is modeled as a function of temperature following Schiller and Finger (2019), and the results show that $aTiO_2$ remains at approximately 0.5±0.05 at <880-900 °C (Fig. S5). This is consistent with the previous estimation of ~0.5 for ilmenite-bearing silicic magmas (Ferry and Watson 2007; Schiller and Finger 2019). We thus use an $aTiO_2$ of 0.5 for the ilmenite-bearing peraluminous rocks, and this may introduce uncertainties of <10 °C. The case of 0.75 is also tested to show how the estimated temperature varies as a function of $aTiO_2$. $aSiO_2$ (generally >0.9 for high-silica magmas) has a small influence of <10 °C (Schiller and Finger 2019); thus, we use an $aSiO_2$ of 1. Pressure increases the calculated Ti-in-zircon temperature by 5-10 °C per 100 MPa (Ferry and Watson 2007; Ferriss et al. 2008). In contrast, the increase in pressure results in higher $aTiO_2$ values (Fig. S5) and thus decreases the Ti-in-zircon temperatures. The two contrasting effects can be roughly counteracted, e.g., the decrease in pressure from 500 MPa to 150 MPa leads to decreases of 18-35 °C for temperature and a decrease of ~0.08 for $aTiO_2$ (corresponding to an increase of ~20 °C, Fig. S6). Pressure thus likely has an influence of <15 °C on the estimation of Ti-in-zircon temperature.

Overall, these uncertainties added to the calibration and analytical uncertainties of ~20 °C result in a total maximum uncertainty of ~55 °C for single-grain zircon. This estimate is larger than the previous evaluation of 20-30 °C (Schiller and Finger 2019), which does not incorporate the pressure effect. The uncertainty of a set of data will be decreased if the crystallization has a normal temperature distribution, which can be characterized by the median/average value (Fig. 11). The standard error (equivalent to the root mean square error, Putirka 2008) on the median/average temperature is typically <20 °C if >10 grains are effectively analysed.

The calculated Ti-in-zircon temperatures are evaluated by comparison with zircon saturation temperature (T_{sat}). Because of the occurrence of inherited zircons in the S-type rocks, T_{sat} is approximated by the approach of Schiller and Finger (2019), which is based on "zircon crystallization temperature distribution" from zircon saturation model and whole-rock chemistry data. The approach suggests that T_{sat} is higher than the median Ti-in-zircon temperature by a constant value (generally 35-50 °C) for a given sample, independent of absolute Zr content or melt temperature (Schiller and Finger 2019). Those zircon crystals with higher Ti-in-zircon temperatures than T_{sat} may represent antecrysts or inherited crystals, which are not taken into consideration. For the Banba rhyolite, zircon core and rim Ti contents yield median temperatures of 836±32 °C and 861±36 °C (the ±32 and ±36 °C are two standard deviations denoting the crystallization interval of zircon; Fig. 11a) with standard errors of ±20 °C and ±13 °C on the medians, respectively. For the Taima and Dasi porphyries and the Jiuzhou charnockite, the median temperatures are 824±36 °C, 818±40 °C, and 809±52 °C (Fig. 11a) with standard errors of ±8 °C, ±10 °C, and ±10 °C on the medians, respectively. At a higher $aTiO_2$ of 0.75, the Ti-in-zircon temperatures are overall ~40 °C lower than the case of $aTiO_2$ of 0.5 (Fig. 11b).

Thermodynamic modeling

Thermodynamic modeling could be applicable for magmas that have experienced open-system evolution (e.g., magma recharge) if we can identify an equilibrium subset of the bulk rock volume (i.e., the reactive magma, Pichavant et al. 2007), which includes the rims of zoned crystals and interstitial melts but excludes the cores of zoned crystals. Since interstitial groundmasses of the studied rhyolite and porphyry units are chemically homogenous (Fig. 9), the reactive magma composition can be reconstructed by subtracting the composition of out-of-equilibrium phenocrysts (OEPs) from the whole-rock composition (Supplementary text S9). The OEPs are dominantly represented by cores of zoned quartz and plagioclase because other phenocrysts (cordierite, orthopyroxene, biotite, and/or alkali feldspar) may have achieved re-equilibration with the interstitial melts, as suggested by their homogenous compositions (Zhao et al. 2017a). Equilibrium may also be attested by the partially well-developed crystal faces for cordierite (Fig. 2f).

For the Banba rhyolite, statistics based on quartz CL images suggest that the amounts of OEPs (Groups B and C quartz) approximate ~25% (relative to phenocryst volume). Owing to the low fraction (<19 vol%) of phenocrysts, the presence of 25% (or even a higher fraction of 50%) OEPs leads to indistinguishable differences between the reactive magma and average whole-rock compositions (71.2-71.3 wt% versus 71.3 wt% SiO_2, respectively; Table S1). For the crystal-rich Taima porphyries, the influence of OEPs should be more prominent than the case of the Banba rhyolite. A series of thermodynamic modeling with variable amounts of OEPs is tested to best fit the measured compositional distribution of plagioclase phenocrysts (Fig. 13c). The results suggest that the modeled plagioclase compositions match the measured compositions by deducting 20-30% OEPs from the average whole-rock composition (Fig. 13c; Table S1). Similar amounts of OEPs (~20%) can be estimated from statistics based on quartz CL and plagioclase BSE images. Additional uncertainties may be introduced owing to the use of the average whole-rock composition. Reconnaissance modeling using sample compositions with the highest and lowest SiO_2 contents shows that the selection of average whole-rock compositions influences the temperature and melt fraction by only <5 °C and <5 vol%, respectively. The reconstructed compositions of reactive magmas and the volume fraction and composition of the OEPs used in the calculation are provided in supplementary text S9 and table S1.

For the Banba rhyolite, the modeled phase relations are shown to cover the pressure range of 50-150 MPa, which is independently constrained by fitting the evolution trend of melt inclusions (using Rhyolite_MELTS software; see more in Fig. 9). This approach represents a qualitative estimation because pressure mildly influences phase relations (e.g., slope of the phase stability field boundaries, Figs. 12 and 13) and thus liquid evolution (e.g., Melekhova et al. 2015). Quantitative estimation of pressure is not obtained, as the melt inclusions do not represent cotectic melts (Fig. 9). The phase relations are further combined with Ti-in-zircon thermometric results to explain petrographic observations. The absence of alkali feldspar and the presence of <19% phenocrysts in the Banba rhyolites are best explained by the case with $aTiO_2$ of 0.5 and system H_2O content of 1.5% (Fig. 12b; Supplementary text S9). The estimation of $aTiO_2$ in this way is consistent with the above constraints on $aTiO_2$. The crystallization temperature intervals of quartz and zircon largely overlap at a pressure range of 50-150 MPa for the Banba magma (Fig. 12b).

For the Taima porphyry, the previous two-feldspar equilibrium temperature of ~830±50 °C at 200 MPa requires system H_2O contents of >1 wt% (Zhao et al. 2017a). The stability of alkali feldspar and orthopyroxene and the presence of 28-48% phenocrysts are best explained by the results with $aTiO_2$ of 0.5 and system H_2O content of 1.5% (Fig. 13; Supplementary text S9). In this case, the crystallization temperature intervals of quartz and zircon also overlap at a pressure range of 50-150 MPa for the Taima porphyritic magma (Fig. 13a).

Ti-in-quartz thermobarometry

The Ti-in-quartz thermobarometer has been calibrated by many experiments (Thomas et al. 2010; Huang et al. 2012; Zhang et al. 2020; Osborne et al. 2022). The calibration by Zhang et al. (2020) is adopted here because other calibrations yield either significantly higher pressure (>300 MPa; Thomas et al. 2010; Osborne et al. 2022) or lower pressure (<50 MPa; Huang et al. 2012) at comparable temperatures (Fig. S6). This thermobarometer yields pressure within an uncertainty of ±20 MPa, assuming an input temperature uncertainty of ±25 °C (Zhang et al. 2020).

Since the crystallization temperature intervals of quartz and zircon largely overlap, we could use the Ti-in-zircon temperature as input to obtain the pressure conditions from the Ti-in-quartz thermobarometer. For the Banba rhyolite, zircon crystals develop reverse zonation characterized by slightly Ti-rich and bright rims (Fig. S3). Accordingly, quartz crystals also have reverse zonation, where the Ti-rich Group A quartz is present as a bright rim surrounding the Group B quartz (sometimes the Group C quartz). Therefore, the crystallization temperature intervals of the Groups A and B quartz in the Banba rhyolite may be represented by the temperature intervals of zircon rims and cores, respectively. The Groups A and B quartz in the Banba rhyolite thus should crystallize at ~60±20 MPa and ~150±40 MPa, respectively (Fig. 14a;

±20 and ±40 MPa denote the pressure uncertainties introduced by the standard errors of 13 °C and 20 °C on the median Ti-in-zircon temperature). The crystallization pressure of Group B quartz is approximate to the pressure conditions (50-150 MPa) at which melt inclusions hosted by Group B quartz evolved (Fig. 9), thereby suggesting the self-consistency of our approach. Within the temperature interval represented by zircon cores, the Group C quartz with the lowest Ti contents crystallizes at a high pressure of 600±80 MPa (Fig. 14a), which should be underestimated because quartz should have crystallized prior to zircon at pressures of >150 MPa (Fig. 12b).

For the Taima and Dasi porphyries, as zircon cores and rims do not show distinguishable compositional differences, we assume that the Groups A and B quartz crystals crystallize at similar temperature intervals represented by the Ti-in-zircon temperatures, and thus, the corresponding pressures are estimated at 30±10 MPa and 110±20 to 140±20 MPa, respectively (Fig. 14a; with standard errors of 8-10 °C on the median Ti-in-zircon temperatures). Similar to the case of the Banba rhyolite, Group C quartz in the porphyries likely crystallizes at >500-550 MPa, as the temperature may be higher than the Ti-in-zircon temperature. At a higher $aTiO_2$ of 0.75, the estimated pressures for these units will increase to ~100±20 MPa, ~150±40 to ~220±40 MPa, and >550 MPa for Groups A, B and C crystals (Fig. 14b).

Discussion

Evaluating the influence of hydrothermal alteration

Many ancient volcanic and plutonic rocks are inevitably subjected to hydrothermal alteration, which should be evaluated before the application of whole-rock data (e.g., Lackey et al. 2008). Careful petrographical examination under the microscope suggests variable types of mineral-scale alteration, e.g., saussuritization and carbonatization of plagioclase in the Banba rhyolite (Fig. S1b). To address the alteration problem, we use zircon as a benchmark to evaluate the degree of subsolidus hydrothermal alteration and its influence on whole-rock composition.

Published zircon $\delta^{18}O$ values have a wide range of 9-13‰ (mostly 9-10.5‰, with 2σ error of ±0.36‰) for the Banba rhyolites and 10.5-12.5‰ for the Taima porphyries (Jiao et al. 2015). Following the method of Lackey et al. (2008), the whole-rock $\delta^{18}O$ in equilibrium with the zircon $\delta^{18}O$ was calculated at 10.3-12.0‰ for the Banba rhyolite and 11.8-14.0‰ for the Taima porphyry (Supplementary text S10). The calculated whole-rock data largely overlap with the measured whole-rock data, with the exception of one sample (BB01) with a $\delta^{18}O$ value of 9.4‰, which is slightly lower than the $\delta^{18}O$ values of the other samples (Fig. 10b). Therefore, alteration of the rhyolite and porphyry likely remains a closed system. Alternatively, the rocks were subject to open-system alteration at relatively high temperatures, leading to depletion of rocks with respect to ^{18}O, while the ^{18}O depletion may be counteracted by an overprint of low-temperature weathering (Bindeman 2008).

The influence of alteration is further examined on the K/Al versus (2Ca + K + Na)/Al diagram (Fig. 15a; Warren et al. 2007), which shows compositions of common altered minerals (kaolinite, chlorite, illite, K-mica, and zoisite) and primary magmatic minerals (alkali feldspar and plagioclase). The examination suggests that the compositions of volcanic and plutonic samples do not vary following the trend of Ca-Na loss, although two tuff samples lie on the line of Ca-Na loss and two lava samples approach the line (Fig. 15a; the four samples thus are not taken into consideration). Moreover, compared to melt inclusion compositions, the whole-rock compositions of the Banba rhyolite have lower Al_2O_3 (Fig. 9a) and higher CaO (Fig. 9d) contents, and such variations are inconsistent with the effect of plagioclase alteration. Therefore, we posit that the observed alteration probably maintains a close-system process and barely changes the whole-rock major compositions of the volcanic and plutonic samples.

The origin of the crystal-poor, peraluminous rhyolites

It is of significant interest to reconstruct the petrogenetic processes involved in the plumbing system of the Banba rhyolite before the exploration of volcanic-plutonic relationships.

Magma plumbing system. Quartz crystals from the rhyolite and porphyry units have widely variable Ti contents, which may reflect multiple origins of quartz (e.g., the involvement of xenocrysts, Watt et al. 1997) and/or large variations in temperature (Tavazzani et al. 2020) and pressure (Breiter et al. 2012). The Dasi porphyry and the Jiuzhou pluton contain quartz-bearing metasedimentary xenoliths (e.g., gneiss and schist) that are captured from the country rocks during ascent (Zhao et al. 2017b). Quartz crystals in these xenoliths contain abundant mineral inclusions (biotite and plagioclase) and have different compositions (Al and Fe) from quartz in the rhyolite and porphyry units (Fig. 4). Therefore, quartz in the rhyolite and porphyry units may not represent xenocrysts from the country rocks but primary minerals crystallized from magmas with systematically variable compositions.

The Banba quartz crystals develop inverse zonation characterized by a rimward increase in Ti contents (generally >100 ppm, up to 250 ppm, Fig. 5a), which may be caused by a major heating event that increases the temperature by >120 °C (Fig. 11c; Tavazzani et al. 2020). However, the elevated temperature of >900 °C is too high to stabilize quartz (Fig. 12b). Moreover, the small variation in zircon Ti contents from 12.7±1.9 ppm for cores to 15.2±2.0 ppm for rims indicates an increase of only ~25 °C, which is indistinguishable within uncertainties. Therefore, we posit that the Banba magma may be slightly heated by a thermal event, as suggested by the bright rims of zircon in CL images (Supplementary Fig. S3), but the thermal event is not sufficient to account for the large variations in quartz Ti contents, which require to incorporate variations in pressure.

If we use the Ti-in-zircon temperatures to define the main crystallization interval, the Groups A, B, and C quartz crystals in the Banba rhyolites may crystallize at 60±20 MPa, 150±40 MPa, and >600±80 MPa, respectively (Fig. 14a). The pressure conditions are approximate to the pressures of 30±10 MPa, 110-140 MPa, and >500-550 MPa estimated for Groups A, B, and C quartz in the porphyry (Fig. 14a). The estimated pressure conditions largely depend on the calibration of the thermobarometers, while the relative pressures of different groups of quartz would not be changed. These constraints thus manifest the polybaric storage of volcanic-plutonic magmas at upper (2-5 km) and middle (>15-20 km; rock density of 2700 kg/m^3) crustal levels. The inferred plumbing system is consistent with the polybaric storage at ~50-150 MPa and ~400-550 MPa for the porphyry proposed by Charoy and Bernard (2008) based on mineral stability. The shallow storage conditions estimated for the Banba rhyolite are not rare for rhyolites around the globe (e.g., 40-100 MPa for the Novarupta rhyolite, Alaska, Coombs and Gardner 2001; 50-100 MPa for the Cordón Caulle rhyolite, Chile, Castro et al. 2013). Magmas stored in the middle crust have started to crystallize Group C quartz at relatively high temperatures because the quartz saturation temperature increases to >900 °C at pressures of >400 MPa for H_2O-poor systems (<2 wt%; Clemens and Philips 2014). The middle crust reservoir may also involve extensive melting of metasedimentary rocks, as suggested by the presence of strongly peraluminous restitic granulite enclaves (~500±80 MPa to ~675±25 MPa; Zhao et al. 2017b). Extensive melting of the metasedimentary rocks may be caused by the intrusion of large volumes of magmas that are derived from deeper crust. This scenario has been well documented in the central Andean Puna

Plateau (e.g., the peraluminous Coyaguayma and Ramadas rhyolites, Caffe et al. 2012; Coira et al. 2018).

Magma hybridization in the middle crust. Peraluminous rhyolites may not represent pure, metasediment-sourced melts but contain important contributions of mantle-derived or metaigneous-sourced magmas (e.g., Dokuz et al. 2017; Coira et al. 2018). For the Banba rhyolite, the involvement of mantle-derived or metaigneous-sourced magmas is supported by the less evolved compositions of zircon (Fig. 8), lower initial $^{87}Sr/^{86}Sr$ ratios, higher $\varepsilon_{Nd}(t)$ values, and lower $\delta^{18}O$ values (Fig. 10a, b) than those exhibited by the nearby S-type Jiuzhou granites. The similar Fe contents of Groups B and C quartz suggest that the magmas from which the Group B quartz crystallizes may be directly derived from the middle crustal reservoir. The melt inclusions hosted by the Group B quartz (Fig. S7) thus may record direct information on magma composition in the middle crust.

The melt inclusions are more enriched in Cl (190-2050 ppm) than in F (<320 ppm). The volatile component is different from the volatile of a metasediment-sourced magma, which is dominated by F over Cl (London 1997). A Cl-rich component is thus required to interpret the volatile budget. Arc basaltic magmas represent a great potential source of Cl (500-2000 ppm; Zellmer et al. 2015; Kendall-Langley et al. 2021), but hybridization between rhyolitic and basaltic magmas generally requires high proportions (>40%) of mafic endmembers, thus producing less felsic hybrids (<70 wt% SiO_2; Laumonier et al. 2014) than the Banba rhyolite. The Sr-Nd-O isotopes with a signature of reworked crust (Fig. 10) also preclude basaltic magmas as an endmember of hybridization. Therefore, the Cl-rich magma is more likely to be derived from fractionation and assimilation of the arc basaltic magmas (Kendall-Langley et al. 2021) or from partial melting of a crustal source (e.g., metatonalite and/or metabasalt; Farina et al. 2014).

Regionally, amphibole-bearing dacites (~246±2 Ma) with $\varepsilon_{Nd}(t)$ values of -9.6~-9.0 outcrops at ~100 km northwest of the Banba rhyolite unit (Qin et al. 2011) and may represent a potential endmember of hybridization. We use the amphibole-bearing dacites and the S-type late Jiuzhou granites as endmembers to model the mixing trend, which is consistent with the main variation trend of the Sr-Nd isotope data for the studied volcanic and plutonic rocks (Fig. 10a). The metaluminous melt inclusions in the Banba rhyolite suggest that hybridization in the middle crust likely produced metaluminous melts. The feature of the peraluminous whole-rock compositions then presents a special interest. A similar case has been reported for the peraluminous rhyolite from the Streltsovka caldera, where the melt inclusions are mildly peralkaline (Chabiron et al. 2001). For the Banba rhyolite, we posit that entrainment of cordierite from the melting metasedimentary source in the middle crust may be an important process to produce peraluminous whole-rock compositions. Melting of metasedimentary rocks can be supported by the presence of cordierite-rich restitic granulite enclaves that record high temperatures of >900 °C (Zhao et al. 2017b). This interpretation is also supported by the positive relationship between whole-rock ASI and FeO+MgO contents (Fig. S8; Stevens et al. 2007).

Magma recharge into a shallow evolved magma reservoir. The trace element contents of quartz and zircon are sensitive to recharge events (e.g., Wark et al. 2007; Yan et al. 2020). For the Banba rhyolite, the Ti-rich bright rims of quartz (Group A crystals, Fig. 5a) and zircon (Fig. S6) likely formed in response to magma recharge into the upper crustal reservoir. This recharge event is more clearly supported by the quartz Fe contents, i.e., the Group A quartz crystals in the Banba rhyolite have apparently higher Fe contents (100-200 ppm versus <100 ppm) than the Groups B and C quartz crystals (Fig. 4b). This feature is unlikely to be related to a fractionation or assimilation process but can be better interpreted by recharge and subsequent mixing with a less evolved magma at the shallow level (~60±20 MPa).

The thermal feasibility of the mixing process at such a shallow level could be evaluated by estimating the cooling timescale of the Banba system. Efficient mixing occurs when the recharge magma is brought rapidly into contact with the host magma, or at least over a time period during which cooling of the host magma is minor; otherwise, the high viscosity of the highly crystalline mush will inhibit mixing (Laumonier et al. 2014). The modeled median timescale for quartz residence in the shallow reservoir is 30 kyrs (with 2σ uncertainty of 72 kyrs) if the temperature is represented by the maximum Ti-in-zircon temperature of 897 °C, while the median timescale increases to 180 kyrs (with 2σ uncertainty of 432 kyrs) if a minimum temperature of 825 °C is used (Supplementary table S3). In either case, the maximum timescale (102 kyrs or 612 kyrs) is significantly shorter than the critical timescale of 1500-2000 kyrs required to freeze the Banba magma body with a volume of 750-1500 km^3 (Fig. S9; Laumonier et al. 2014; volume estimation assuming a depth range of 1.5-3.0 km, corresponding to a pressure range of 40-80 MPa, and an area of the reservoir on the order of 500-1000 km^2, Fig. 1b). Therefore, the shallow reservoir could maintain a largely molten state to allow for efficient mixing. In fact, magma recharge and mixing processes have also been documented by other shallow reservoirs, e.g., the 1.8–4.4 km Novarupta subvolcanic reservoir (Coombs and Gardner 2001; Singer et al. 2016).

The recharge and subsequent mixing event pose a challenge to understanding the relationship between the shallow (~60±20 MP) and deeper (~150±40 MP) reservoirs, which could be explored by examining the variations in whole-rock and melt inclusion compositions. The large compositional variation exhibited by the melt inclusions can be fitted by the modeled fractionation trend of a parental melt represented by the least evolved melt inclusion

(Rhyolite_MELTS modeling, Gualda et al. 2012a; Fig. 9), although the modeling fails to reproduce the variation in Na_2O and CaO of melt inclusions. This failure is likely related to the overestimation of the plagioclase saturation temperature by the Rhyolite_MELTS modeling (Gardner et al. 2014). The magmas derived from the middle crustal reservoir thus likely experienced extensive fractionation during storage in the upper crustal reservoir. However, the variations in the whole-rock compositions largely deviate from the fractionation trend of melt inclusions (Fig. 9). At comparable SiO_2 contents, the bulk rocks have lower Al_2O_3, Na_2O and K_2O contents (Fig. 9a, e, f) but higher FeO, MgO and CaO contents (Fig. 9b, c, d) than the melt inclusions. This compositional feature can be interpreted by a mixing process between a less evolved recharge magma and a segregated melt. As the melt inclusions are mostly sealed by Group B quartz (Fig. S7), the melt inclusions are not influenced by the late recharge/mixing process in the shallow reservoir, while the bulk rocks incorporate a higher fraction of less evolved recharge magmas. This interpretation may be applicable to other rhyolites with similar compositional features, e.g., the Aniakchak rhyolite from Alaska (Larsen 2006) and the Toba rhyolite from Indonesia (Chesner and Luhr 2010; Fig. S10). Especially for the Toba rhyolite, textural analyses of quartz suggest that melt inclusions typically occur in dark cores but seldom in bright rims (Barbee et al. 2020), a feature similar to the case of the Banba rhyolite.

To reproduce the variation trend of whole-rock compositions, one endmember of magma mixing represented by the melt inclusion compositions should be located at the compositional trend defined by the whole-rock composition. Hence, the low-silica melt inclusions (e.g., with ~70-74 wt% SiO_2) are not appropriate because they have deviated from the trend of whole-rock composition (Fig. 9). The most likely candidates are melt inclusions clustered at 74-76 wt% SiO_2 (Fig. 9). Thermodynamic modeling suggests that these melt inclusions with 74-76 wt% SiO_2 may represent interstitial melts after ~50-60% crystallization of the parental melts (with ~70 wt% SiO_2). If these interstitial melts do not segregate with the highly crystalline mush, efficient mixing with recharge magmas should not take place because of the large rheological difference (Laumonier et al. 2014). Therefore, melt extraction should have played an important role in the formation of the Banba rhyolite. Mass balance calculations suggest that the Banba whole-rock compositions can be reproduced by incorporating ~50-60% dacitic recharge magmas and ~40-50% segregated melts with <30% phenocrysts (Fig. 15; see supplementary text S11 for modeling details; Zhao et al. 2018; Farina et al. 2020).

The development of the crystal-rich porphyries

Porphyry, consisting of fine-grained groundmass and coarser phenocrysts, represents an important unit in many volcanic-plutonic (or caldera) complexes (e.g., Deering et al. 2016; Yan et al. 2018, 2020; Tavazzani et al. 2020). Exploring the magmatic processes of porphyry is thus key to evaluating the link between volcanic and plutonic rocks.

Magma plumbing system. Thermobarometric results suggest that the porphyritic magmas were derived from a deep crustal reservoir at >450-550 MPa (corresponding to >14-15 km) and stored in an upper crustal reservoir at ~110±20 MPa to 140±20 MPa (corresponding to ~3.0-5.2 km). The porphyritic magmas then ascended and emplaced at ~30±10 MPa (~1 km; Fig. 14a). The ultrashallow emplacement is consistent with the field and textural features of the Taima and Dasi porphyritic cryptodomes. Columnar jointing (Fig. 3a), resulting from contraction during rapid cooling of magmas, is a common feature in many ultrashallow cryptodomes (e.g., the Milos cryptodome from Greece, Stewart and McPhie 2003). The presence of autoclastic fragments of feldspar and quartz (Fig. 3a) is believed to be caused by energy release due to exsolution of an aqueous fluid phase in an ultrashallow environment (Burnham 1985; Taisne and Jaupart 2011). The low-anorthite plagioclase overgrowth (~$An_{27\text{-}40}$; Fig. 7b) and groundmass (~$An_{30\text{-}42}$; Fig. 7c) also suggest crystallization at low melt H_2O contents after degassing of H_2O-saturated magmas (e.g., McCanta et al. 2007). Thermodynamic modeling predicts that H_2O saturates at pressure conditions of <40-45 MPa (Fig. 13a), consistent with the Ti-in-quartz thermobarometric results.

Magma recharge and convection in the upper crustal reservoir. Plagioclase phenocrysts may record instantaneous changes in the composition and/or temperature of magma reservoirs in response to magma recharge due to the sluggish diffusion of the NaSi–CaAl couple in plagioclase (e.g., Grove et al. 1984). However, the sensitivity of the plagioclase recorder is influenced by H_2O contents, as suggested by crystallization experiments (Prouteau and Scaillet 2003; Huang et al. 2019) and thermodynamic modeling (Fig. 13c). For H_2O-poor magmas, plagioclase anorthite content has a small variation in response to a given temperature fluctuation (Fig. 13c). For the Taima porphyry with 1.5 wt% initial melt H_2O contents, plagioclase is predicted to have a compositional variation of only ±2 mol% An corresponding to the Ti-in-zircon temperature range of 824±36 °C (Fig. 13c). The modeled composition variation is consistent with the weakly zoned or unzoned feature of the plagioclase phenocrysts in the porphyries, which provides limited information on magma processes.

A small portion (<20%) of plagioclase phenocrysts develop small scales of resorptions (at ~5-10 μm spacing) and oscillations (at ≤5-7 mol% An; Fig. 6a, d). If these zoned plagioclase phenocrysts represent autocrysts that crystallized from the magmas, the high-frequency and small-amplitude oscillatory zonation generally implies mixing or convection with local-scale, large thermal fluctuation (Ginibre et al. 2002, 2007), rather than kinetic effects at the crystal–

melt interface under a stagnant environment, which could not explain the resorption surfaces here (Fig. 6c; Ginibre et al. 2007). Some plagioclase phenocrysts have broader resorption zones at ~40-50 μm spacing, although the compositional oscillation at ~5-7 mol% An is not more prominent (e.g., Fig. 6b, c, e, f). Such oscillatory zonation may be explained as a result of convection at the chamber scale (Ginibre et al. 2002) or recharge of magma that is slightly different in temperature or composition (Pizarro et al. 2019; Magee et al. 2020). Convection in the magma chamber is driven by density instability due to the temperature/crystallinity gradient in the reservoir, which may be related to either magma cooling from above (Hort et al. 1999) or recharge of a new magma into a preexisting magma chamber (e.g., Huber et al. 2009). The former case is not favored here because the roofward decline in mineral (e.g., quartz and alkali feldspar) liquidus temperature prevents significant crystallization against the roof (see crystallinity isopleths with positive slopes in Fig. 13; Hildreth and Wilson 2007), and potential settling of denser crystals may also decrease the thickness of the mushy layer at the roof (e.g., Bachmann and Bergantz 2004). Therefore, recharge and subsequent convection seem to be correlative processes (Huber et al. 2009).

If the zoned plagioclase phenocrysts represent antecrysts of a pre-existing reservoir or xenocrysts introduced during open-system evolution, the recharge process is not evidenced by plagioclase zonation. Nevertheless, the recharge event is further supported by the pervasive resorption of quartz and alkali feldspar (Fig. 3c, d; Wark et al. 2007; Chamberlain et al. 2015). Recharge of a hot magma could heat the porphyritic magmas and lead to significant remelting of quartz and alkali feldspar in the reservoir. Resorption of quartz and alkali feldspar may be enhanced during ascent of porphyritic magmas as a nearly adiabatic ascending path partly comes across the instability field of quartz and alkali feldspar (see dashed line with arrow in Fig. 13a;

Nelson and Montana 1992). Overheating above the liquidus temperature of quartz and alkali feldspar may result in resorption of the two phases (Nelson and Montana, 1992). However, quartz trace elements fail to record the composition of the recharge magmas because the Group B quartz does not have elevated Fe contents, as in the case of the Group A quartz in the Banba rhyolite. The reason may be related to the high viscosity of the crystal-rich porphyritic magmas, which inhibits efficient mixing with the recharge magma (Laumonier et al. 2014). This interpretation is evidenced by the presence of microgranular enclaves in the porphyries (Charoy and Barbey 2008), indicating a mingling process.

Zircon crystals do not record a heating event because the temperature may increase by a small amplitude (likely <20 °C, corresponding to ~2 ppm error on Ti analyses), while magma crystallinity could decrease by ~15 vol% (Fig. 13a). Alternatively, the magma may be significantly heated and become undersaturated with respect to zircon at >859-874 °C (Fig. 11a). Under such conditions, quartz and alkali feldspar should be totally resorbed (Fig. 13a), a feature that is inconsistent with the observations. Zircon crystals in the Taima and Dasi porphyries do not show less evolved compositions than those exhibited by the S-type late Jiuzhou granites (Fig. 8), and the porphyries also do not have apparently lower initial $^{87}Sr/^{86}Sr$ ratios and higher $\varepsilon_{Nd}(t)$ values than the late Jiuzhou granites (Fig. 10a). The presence of microgranular enclaves with SiO_2 contents of 68.3-76.0 wt% and strongly peraluminous compositions in the porphyries (Charoy and Barbey 2008) suggest that the recharge magmas may be derived from partial melting of a metasedimentary source. As the melting temperature recorded by the restitic granulite enclaves is high (>900 °C, Jiao et al. 2013; Zhao et al. 2017b), the hot recharge magmas could remelt and stir the highly crystalline mush.

Exploring the possible connection of the volcanic-porphyritic-hypabyssal units

The key to exploring volcanic-plutonic connection is to examine whether the volcanic and plutonic units have complementary cumulate-liquid geochemistry and form simultaneously (e.g., Deering et al. 2016; Yan et al. 2016, 2018). For the studied QBGC, the whole-rock compositions do not show evidence of cumulate-liquid pairs (Figs. 9 and 10). Moreover, the available field relationship reveals the sequential development of these units. The Banba rhyolite likely erupted prior to the emplacement of the Taima porphyry (Fig. 1c; Yang et al. 2011). The Taima porphyry resembles the early Jiuzhou monzogranite in compositions of major elements (Fig. 9a-f) and Sr-Nd isotopes (Fig. 10a). Thus, the early Jiuzhou monzogranite may represent the deep equivalent of the Taima porphyry. The intrusion of the late Jiuzhou granites into the early Jiuzhou monzogranites (Fig. S3) suggests that the porphyry formed prior to the emplacement of the late Jiuzhou granites. Therefore, a possible temporal sequence is that volcanic eruption was followed by the formation of porphyries, and the pluton experienced two-stage construction with first-stage magmatism contemporary with the porphyries. A direct/tight connection is thus precluded, and we rigorously explore the possible connection among these units in the following.

A spatial variation model: tenuous connection among the coexisting units. The simplest way to interpret these observations on temporal sequence and geochemical features is that the plumbing systems feeding these units are horizontally independent or vertically discrete. The different compositions of these units may be caused by the different source compositions and/or the different magmatic processes. The Banba rhyolites were produced by hybridization between dacitic magmas and metasediment-sourced magmas. The bulk compositions of the Taima and Dasi porphyries and the late Jiuzhou granites have been suggested to be influenced by processes of restite entrainment and crystal accumulation (Zhao et al. 2017b, 2018). Therefore, these complex processes highlight that it is not reliable to explore the relationship among these units on the basis of whole-rock compositions.

Quartz trace elements (especially Al and Fe) potentially provide an effective mineralogical record to assess the assumption of independent plumbing systems. The variations in Al and Fe contents of quartz are controlled by parental magma composition and magma processes (e.g., crystallization/fractionation and mixing, Breiter et al. 2012). As Al and Fe are highly incompatible elements in quartz (with similar partition coefficients of 250-500 and 200-400, respectively, estimated through our analyses of quartz and melt inclusion compositions, supplementary tables S1 and S2), the slope of quartz Al and Fe variation trend should remain largely unchanged during crystallization/fractionation of cognate magmas. Quartz Fe and Al contents for the late Jiuzhou pluton exhibit a different trend from other volcanic and plutonic units (Fig. 4c), implying an independent origin for the former. This interpretation is also supported by the distinct whole-rock Sr-Nd and zircon O isotopic compositions for the late Jiuzhou pluton (Fig. 10). The same evolution trend defined by quartz crystals from the Banba rhyolite, Taima and Dasi porphyries, and early Jiuzhou monzogranite likely suggests that similar parental magmas for these units have experienced similar crystallization/fractionation processes, although the part of the Group A quartz crystals in the rhyolite deviates from the evolution trend owing to the influence of recharge (Fig. 4b, c). The lower Fe and Al contents of quartz in the early Jiuzhou monzogranites than in the rhyolite and porphyry units likely reflect that quartz in the monzogranites dominantly crystallizes or equilibrates under near solidus conditions. The same evolution trend of the rhyolite, porphyry, and monzogranite units leads to the proposal of an alternative model that illustrates their potential link.

This is the peer-reviewed, final accepted version for American Mineralogist, published by the Mineralogical Society of America.
The published version is subject to change. Cite as Authors (Year) Title. American Mineralogist, in press.
DOI: https://doi.org/10.2138/am-2022-8642. http://www.minsocam.org/

A temporal evolution model: cryptic connection among coexisting units. The volcanic-plutonic units may have experienced long-term open-system evolution in a plumbing system. At the earliest stage, hybridization between metasediment-sourced and dacitic magmas produced Cl-rich, metaluminous magmas at the middle crustal level (>15-20 km; Fig. 16a). The magmas ascended upward and assembled to form an upper crustal reservoir covering a maximum depth range of 3.7-7.0 km (i.e., 120±20 to 150±40 MPa; Fig. 16a). Liquid-crystal segregation in the reservoir produced more evolved, crystal-poor melts (Bachmann and Bergantz 2004; Schaen et al. 2018), which further ascended and emplaced at 1.5-3.0 km (corresponding to ~60±20 MPa; Fig. 16a). The dacitic recharge magmas may directly inject into the shallow reservoir without influencing the deeper one (Fig. 16a), thereby resulting in the elevated Fe contents in Group A quartz (Fig. 4b). Another possible configuration for the upper crustal magma system is that the magmas assembled to form a unified large reservoir covering a maximum depth range of 1.5-7.0 km (i.e., 60±20 to 150±40 MPa). Liquid-crystal segregation occurs to produce a zoned mushy reservoir, and the dacitic recharge magmas may traverse the lower mushy layer to inject into the melt-rich cap, as shown by some granite intrusions (Bachl et al. 2001; Shaw and Flood 2009; Zieg and Marsh 2012) and numerical models (e.g., Galetto et al. 2017). While the separate groups of quartz in Ti contents (Fig. 4a) and pressure conditions (Fig. 14a) are better interpreted by the spatial configuration with multiple magma bodies in the upper crust.

After the eruption of the rhyolitic magmas, the unerupted magmas are still stored at depths of ~5.0±1.3 km, which are similar to the depths of the Taima and Dasi porphyries (3.6-5.0 km; Fig. 14a). The Taima and Dasi porphyries thus may form through remobilization of the unerupted mushy layer of the Banba reservoir, although the compositions of porphyries deviate from the modeled cumulate compositions of the Banba melts (Fig. 15b-f). The deviation may be

This is the peer-reviewed, final accepted version for American Mineralogist, published by the Mineralogical Society of America.
The published version is subject to change. Cite as Authors (Year) Title. American Mineralogist, in press.
DOI: https://doi.org/10.2138/am-2022-8642. http://www.minsocam.org/

because the porphyries contain other components, such as restites from the middle crustal melting zone (Zhao et al. 2017b) and quartz crystals from deep reservoirs. The remobilization of the highly crystalline mush is caused by the recharge of hotter metasediment-sourced magmas at the base of the reservoir, subsequently causing convection of the reservoir and mingling between the host and recharge magmas (Fig. 16c). The remobilized magmas ascended upward and reached H_2O saturation below ~50 MPa (Fig. 13a). The release of mechanical energy due to H_2O exsolution broke quartz and feldspar phenocrysts into fragments. Exsolution of H_2O facilitates crystallization of overgrowth surrounding quartz, plagioclase and alkali feldspar at the ultrashallow level (~30±10 MPa; Fig. 16c). Part of the magmas did not evacuate from the mushy reservoir and left a hypabyssal equivalent of the porphyries (i.e., the early Jiuzhou monzogranite), which equilibrates toward near solidus conditions. This model thus better interprets the same variation trend of quartz Fe and Al contents in the rhyolite, porphyry and monzogranite units (Fig. 4b). At the final stage, the mushy reservoir was partly solidified, when new magmas began to intrude the solidified reservoir (as shown by field relations, Fig. S5) and assemble to form the late Jiuzhou body (Fig. 16d).

Implications

This study on the peraluminous QBGC evaluated the obscuring effect of magma recharge on the records of liquid-crystal segregation. This effect poses a challenge to understanding the connection between coexisting volcanic and plutonic units and implies that multidisciplinary constraints should be afforded to comprehensively understand the volcanic-plutonic connection rather than relying only on whole-rock records. The obscuring effect may have a similar impact on understanding the connection of other non-peraluminous volcanic-plutonic systems. For example, the zoned, metaluminous Caetano caldera complex from the Nevada Great Basin was considered to have experienced open-system evolution, e.g., magma recharge and melting of cumulate mush in addition to fractionation; thus, the rhyolite and granitic intrusions have subtle liquid-cumulate geochemistry (Watts et al. 2016). Another example comes from the Yunshan caldera complex, South China, where the compositional change of recharge magmas from metaluminous to peralkaline leads the rhyolites to evolve toward peralkaline compositions with zircon $\delta^{18}O$ values ~1 unit lower than those of metaluminous precursors (Yan et al. 2018, 2020). Xu et al. (2021) also reveal slightly different Nd-Hf isotope compositions between rhyolites and intrusions of the Yunshan caldera complex. Therefore, complex magmatic processes may deviate the volcanic-plutonic units from a cogenetic evolution trend and obscure the original connection of volcanic and plutonic units.

The proposal of cryptic connection has an important impact on understanding the results of big data analyses. These results reveal no compositional differences for global volcanic and plutonic rocks from subduction settings (Glazner, 2015; Keller et al. 2015), thus arguing against a close connection. In rift/hotspot settings, distinguishable differences between volcanic and plutonic rocks have been identified but are considered to be caused by other factors (e.g., reduced eruptibility of hydrous plutonic magmas relative to dry volcanics, Keller et al. 2015) rather than liquid-crystal segregation. Combining the many case studies of individual volcanic-plutonic complexes that clearly show complementary liquid-cumulate geochemistry (e.g., Deering et al. 2016; Yan et al. 2016, 2018), these results raise an outstanding question: how commonly are volcanic silicic magmas physically linked to the underlying plutons? It is probable that magma blurred the original compositional differences of the complementary volcanic-plutonic units. For example, the extracted rhyolitic magmas may be mixed back toward the more primitive parental magmas (Eichelberger et al. 2006), or the residual mush may evolve toward high-silica composition due to recharge of more evolved crustal melts (Eichelberger et al. 2000) and/or digestion of the assimilated country rocks (Erdmann et al. 2009). If these cryptically connected volcanic-plutonic units are classified as unlinked cases, the true connection and thus the important role of crystal-mush extraction in differentiating the continental crust will be largely underestimated. Therefore, comprehensive research integrating multidisciplinary approaches should be conducted to evaluate how important roles complex magmatic processes have played in the modification of the original cumulate-liquid geochemistry.

Acknowledgments

We would like to sincerely thank Editor Allen Schaen and two anonymous reviewers for their many constructive comments and suggestions. Discussions with Olivier Bachmann helped clarify our ideas. We would like to thank Xiao-Yu Liu for their support with cathodoluminescence imaging and Han-Yong Liu, Zhe Chi and En-Nong Tian for their help with the homogenization and analysis of melt inclusions. This work was financially supported by the Natural Science Foundation of China (Grant No. 41903027 and 41930214) and the Fundamental Research Funds for the Central Universities (Grant 0206-14380166).

References cited

Audétat, A., Miyajima, N., Wiesner, D., and Audinot, J.N. (2021) Confirmation of slow Ti diffusion in quartz by diffusion couple experiments and evidence from natural samples. Geology, 49(8), 963-967.

Bachl, C.A., Miller, C.F., Miller, J.S., and Faulds, J.E. (2001) Construction of a pluton: Evidence from an exposed cross section of the Searchlight pluton, Eldorado Mountains, Nevada. GSA Bulletin, 119(9), 1213–1228.

Bachmann, O., and Bergantz, G.W. (2004) On the Origin of Crystal-poor Rhyolites: Extracted from Batholithic Crystal Mushes. Journal of Petrology, 45(8), 1565-1582.

Bachmann, O., and Bergantz, G.W. (2006) Gas percolation in upper-crustal silicic crystal mushes as a mechanism for upward heat advection and rejuvenation of near-solidus magma bodies. Journal of Volcanology and Geothermal Research, 149(1-2), 85-102.

Bachmann, O., Miller, C.F., and de Silva, S.L. (2007) The volcanic–plutonic connection as a stage for understanding crustal magmatism. Journal of Volcanology and Geothermal Research, 167(1-4), 1-23.

Barbee, O., Chesner, C., and Deering, C. (2020) Quartz crystals in Toba rhyolites show textures symptomatic of rapid crystallization. American Mineralogist, 105(2), 194-226.

Bindeman, I. (2008) Oxygen Isotopes in Mantle and Crustal Magmas as Revealed by Single Crystal Analysis. Reviews in Mineralogy and Geochemistry, 69(1), 445-478.

Blundy, J., and Cashman, K. (2008) Petrologic Reconstruction of Magmatic System Variables and Processes. Reviews in Mineralogy and Geochemistry, 69(1), 179-239.

Breiter, K., Svojtka, M., Ackerman, L., and Švecová, K. (2012) Trace element composition of quartz from the Variscan Altenberg–Teplice caldera (Krušné hory/Erzgebirge Mts, Czech Republic/Germany): Insights into the volcano-plutonic complex evolution. Chemical Geology, 326-327, 36-50.

Burnham, A.D. (2020) Key concepts in interpreting the concentrations of the rare earth elements in zircon. Chemical Geology, 551.

Burnham, C.W. (1985) Energy release in subvolcanic environments: implications for breccia formation. Economic Geology, 80, 1515-1522.

Caffe, P.J., Trumbull, R.B., and Siebel, W. (2012) Petrology of the Coyaguayma ignimbrite, northern Puna of Argentina: Origin and evolution of a peraluminous high-SiO_2 rhyolite magma. Lithos, 134-135, 179-200.

Castro, J.M., Schipper, C.I., Mueller, S.P., Militzer, A.S., Amigo, A., Parejas, C.S., and Jacob, D. (2013) Storage and eruption of near-liquidus rhyolite magma at Cordón Caulle, Chile. Bulletin of Volcanology, 75(4).

Chabiron, A., Alyoshin, A.P., Cuney, M., Deloule, E., Golubev, V., Velitchkin, V.I., and Poty, B. (2001) Geochemistry of the rhyolitic magmas from the Streltsovka caldera (Transbaikalia, Russia): a melt inclusion study. Chemical Geology, 175, 273–290.

Chamberlain, K.J., Wilson, C.J.N., Wallace, P.J., and Millet, M.A. (2015) Micro-analytical Perspectives on the Bishop Tuff and its Magma Chamber. Journal of Petrology, 56(3), 605-640.

Charoy, B., and Barbey, P. (2008) Ferromagnesian silicate association in S-type granites: the Darongshan granitic complex (Guangxi, South China). Bulletin de la Société Géologique de France, 179, 13-27.

Chesner, C.A., and Luhr, J.F. (2010) A melt inclusion study of the Toba Tuffs, Sumatra, Indonesia. Journal of Volcanology and Geothermal Research, 197(1-4), 259-278.

Clemens, J.D., and Phillips, G.N. (2014) Inferring a deep-crustal source terrane from a high-level granitic pluton: the Strathbogie Batholith, Australia. Contributions to Mineralogy and Petrology, 168(5).

Coira, B., Kay, S.M., Viramonte, J.G., Kay, R.W., and Galli, C. (2018) Origin of late Miocene Peraluminous Mn-rich Garnet-bearing Rhyolitic Ashes in the Andean Foreland (Northern Argentina). Journal of Volcanology and Geothermal Research, 364, 20-34.

Connolly, J.A.D. (2005) Computation of phase equilibria by linear programming: A tool for geodynamic modeling and its application to subduction zone decarbonation. Earth and Planetary Science Letters, 236(1-2), 524-541.

Coombs, M.L., and Gardner, J.E. (2001) Shallow-storage conditions for the rhyolite of the 1912 eruption at Novarupta, Alaska. Geology, 29(9), 775–778.

Deering, C.D., Keller, B., Schoene, B., Bachmann, O., Beane, R., and Ovtcharova, M. (2016) Zircon record of the plutonic-volcanic connection and protracted rhyolite melt evolution. Geology, 44(4), 267-270.

Dokuz, A., Külekçi, E., Aydınçakır, E., Kandemir, R., Cihat Alçiçek, M., Pecha, M.E., and Sünnetçi, K. (2017) Cordierite-bearing strongly peraluminous Cebre Rhyolite from the eastern Sakarya Zone, NE Turkey: Constraints on the Variscan Orogeny. Lithos, 278-281, 285-302.

Eichelberger, J.C., Chertkoff, D.G., Dreher, S.T., and Nye, C.J. (2000) Magmas in collision: Rethinking chemical zonation in silicic magmas. Geology, 28(7), 603–606.

Eichelberger, J.C., Izbekov, P.E., and Browne, B.L. (2006) Bulk chemical trends at arc volcanoes are not liquid lines of descent. Lithos, 87(1-2), 135-154.

Erdmann, S., Jamieson, R.A., and MacDonald, M.A. (2009) Evaluating the Origin of Garnet, Cordierite, and Biotite in Granitic Rocks: a Case Study from the South Mountain Batholith, Nova Scotia. Journal of Petrology, 50(8), 1477-1503.

Erdmann, S., Wang, R., Huang, F., Scaillet, B., Zhao, K., Liu, H., Chen, Y., and Faure, M. (2019) Titanite: A potential solidus barometer for granitic magma systems. Comptes Rendus Geoscience, 351(8), 551-561.

Farina, F., Dini, A., Rocchi, S., and Stevens, G. (2014) Extreme mineral-scale Sr isotope heterogeneity in granites by disequilibrium melting of the crust. Earth and Planetary Science Letters, 399, 103-115.

Farina, F., Mayne, M.J., Stevens, G., Soorajlal, R., Frei, D. and Gerdes, A. (2020) Phase equilibria constraints on crystallization differentiation: insights into the petrogenesis of the normally zoned Buddusò Pluton in north-central Sardinia. In: Janoušek V Bonin, B., Collins WJ, Farina F, Bowden P, (eds) 2020. Post-Archean Granitic Rocks: Petrogenetic Processes and Tectonic Environments. Geological Society, London, Special Publications, 491, 1, 243-265.

Ferriss, E.D.A.E., and Becker, U. (2008) Computational study of the effect of pressure on the Ti-in-zircon geothermometer. European Journal of Mineralogy, 20(5), 745-755.

Ferry, J.M., and Watson, E.B. (2007) New thermodynamic models and revised calibrations for the Ti-in-zircon and Zr-in-rutile thermometers. Contributions to Mineralogy and Petrology, 154(4), 429-437.

Galetto, F., Acocella, V., and Caricchi, L. (2017) Caldera resurgence driven by magma viscosity contrasts. Nature Communications, 8(1), 1750.

Gardner, J.E., Befus, K.S., Gualda, G.A.R., and Ghiorso, M.S. (2014) Experimental constraints on rhyolite-MELTS and the Late Bishop Tuff magma body. Contributions to Mineralogy and Petrology, 168(2).

Ginibre, C., Kronz, A., and Wörner, G. (2002) High-resolution quantitative imaging of plagioclase composition using accumulated backscattered electron images: new constraints on oscillatory zoning. Contributions to Mineralogy and Petrology, 142(4), 436-448.

Ginibre, C., Wörner, G., and Kronz, A. (2007) Crystal zoning as an archive for magma evolution. Elements, 3, 261–266.

Glazner, A.F., Coleman, D.S., and Bartley, J.M. (2008) The tenuous connection between high-silica rhyolites and granodiorite plutons. Geology, 36(2).

Grove, T., Baker, M.B., and Kinzler, R.J. (1984) Coupled CaAl-NaSi diffusion in plagioclase feldspar Experiments and applications to cooling rate speedometry. Geochemica Cosmochimica Acta, 48, 2113-2121.

Gualda, G.A., Ghiorso, M.S., Lemons, R.V., and Carley, T.L. (2012a) Rhyolite-MELTS: a Modified Calibration of MELTS Optimized for Silica-rich, Fluid-bearing Magmatic Systems. Journal of Petrology, 53(5), 875-890.

Gualda, G.A., Pamukcu, A.S., Ghiorso, M.S., Anderson, A.T., Jr., Sutton, S.R., and Rivers, M.L. (2012b) Timescales of quartz crystallization and the longevity of the Bishop giant magma body. PLoS One, 7(5), e37492.

Hartung, E., Caricchi, L., Floess, D., Wallis, S., Harayama, S., Kouzmanov, K., and Chiaradia, M. (2017) Evidence for Residual Melt Extraction in the Takidani Pluton, Central Japan. Journal of Petrology, 58(4), 763-788.

Hildreth, W. (1981) Gradients in silicic magma chambers: Implications for lithospheric magmatism. Journal of Geophysical Research: Solid Earth, 86(B11), 10153-10192.

Hildreth, W., and Wilson, C.J.N. (2007) Compositional Zoning of the Bishop Tuff. Journal of Petrology, 48(5), 951-999.

Holness, M.B. (2018) Melt segregation from silicic crystal mushes: a critical appraisal of possible mechanisms and their microstructural record. Contributions to Mineralogy and Petrology, 173(6), 48.

Hort, M., Marsh, B., Resmini, R.G., and Smith, M.K. (1999) Convection of crystallization in a liquid cooled from above: an experimental and theoretical study. Journal of Petrology, 40(8), 1271–1300.

Hu, L., Cawood, P.A., Du, Y., Yang, J., and Jiao, L. (2015) Late Paleozoic to Early Mesozoic provenance record of Paleo-Pacific subduction beneath South China. Tectonics, 34(5), 986-1008.

Huang, F., Scaillet, B., Wang, R., Erdmann, S., Chen, Y., Faure, M., Liu, H., Xie, L., Wang, B., and Zhu, J. (2019) Experimental Constraints on Intensive Crystallization Parameters and Fractionation in A-Type Granites: A Case Study on the Qitianling Pluton, South China. Journal of Geophysical Research: Solid Earth, 124(10), 10132-10152.

Huang, R., and Audétat, A. (2012) The titanium-in-quartz (TitaniQ) thermobarometer: A critical examination and re-calibration. Geochimica et Cosmochimica Acta, 84, 75-89.

Huber, C., Bachmann, O., and Dufek, J. (2012) Crystal-poor versus crystal-rich ignimbrites: A competition between stirring and reactivation. Geology, 40(2), 115-118.

Huber, C., Bachmann, O., and Manga, M. (2009) Homogenization processes in silicic magma chambers by stirring and mushification (latent heat buffering). Earth and Planetary Science Letters, 283(1-4), 38-47.

Huber, C., Bachmann, O., and Manga, M. (2010) Two Competing Effects of Volatiles on Heat Transfer in Crystal-rich Magmas: Thermal Insulation vs Defrosting. Journal of Petrology, 51(4), 847-867.

Jiao, S.J., Guo, J.H., and Peng, S.B. (2013) Petrogenesis of garnet in the Darongshan-Shiwandashan granitic suite of the South China Block and the metamorphism of the granulite enclave. Acta Petrologica Sinica, 29(5), 1740-1758.

Jiao, S.J., Li, X.H., Huang, H.Q., and Deng, X.-G. (2015) Metasedimentary melting in the formation of charnockite: Petrological and zircon U-Pb-Hf-O isotope evidence from the Darongshan S-type granitic complex in southern China. Lithos, 239, 217-233.

Karakas, O., Wotzlaw, J.F., Guillong, M., Ulmer, P., Brack, P., Economos, R., Bergantz, G.W., Sinigoi, S., and Bachmann, O. (2019) The pace of crustal-scale magma accretion and differentiation beneath silicic caldera volcanoes. Geology, 47(8), 719-723.

Keller, C.B., Schoene, B., Barboni, M., Samperton, K.M., and Husson, J.M. (2015) Volcanic-plutonic parity and the differentiation of the continental crust. Nature, 523(7560), 301-7.

Kemp, A.I.S., Hawkesworth, C.J., Paterson, B.A., Foster, G.L., Kinny, P.D., Whitehouse, M.J., Maas, R., and Eimf. (2008) Exploring the plutonic-volcanic link: a zircon U-Pb, Lu-Hf and O isotope study of paired volcanic and granitic units from southeastern Australia. Transactions of the Royal Society of Edinburgh: Earth Sciences, 97(4), 337-355.

Kendall-Langley, L.A., Kemp, A.I.S., Hawkesworth, C.J., Craven, J., Talavera, C., Hinton, R., and Roberts, M.P. (2021) Quantifying F and Cl concentrations in granitic melts from apatite inclusions in zircon. Contributions to Mineralogy and Petrology, 176(7).

Lackey, J.S., Valley, J.W., Chen, J.H., and Stockli, D.F. (2008) Dynamic Magma Systems, Crustal Recycling, and Alteration in the Central Sierra Nevada Batholith: the Oxygen Isotope Record. Journal of Petrology, 49(7), 1397-1426.

Larsen, J.F. (2006) Rhyodacite magma storage conditions prior to the 3430 yBP caldera-forming eruption of Aniakchak volcano, Alaska. Contributions to Mineralogy and Petrology, 152(4), 523-540.

Laumonier, M., Scaillet, B., Pichavant, M., Champallier, R., Andujar, J., and Arbaret, L. (2014) On the conditions of magma mixing and its bearing on andesite production in the crust. Nature Communications, 5, 5607.

London, D. (1997) Estimating abundances of volatile and other mobile components in evolved silicic melts through mineral-melt equilibria. Journal of Petrology, 38(12), 1691-1706.

Loucks, R.R., Fiorentini, M.L., and Henríquez, G.J. (2020) New Magmatic Oxybarometer Using Trace Elements in Zircon. Journal of Petrology, 61(3).

Magee, R., Ubide, T., and Kahl, M. (2020) The Lead-up to Mount Etna’s Most Destructive Historic Eruption (1669). Cryptic Recharge Recorded in Clinopyroxene. Journal of Petrology, 61(1).

McCanta, M.C., Rutherford, M.J., and Hammer, J.E. (2007) Pre-eruptive and syn-eruptive conditions in the Black Butte, California dacite: Insight into crystallization kinetics in a silicic magma system. Journal of Volcanology and Geothermal Research, 160(3-4), 263-284.

Melekhova, E., Blundy, J., Robertson, R., and Humphreys, M.C.S. (2015) Experimental Evidence for Polybaric Differentiation of Primitive Arc Basalt beneath St. Vincent, Lesser Antilles. Journal of Petrology, 56(1), 161-192.

Morgavi, D., Laumonier, M., Petrelli, M., and Dingwell, D.B. (2022) Decrypting Magma Mixing in Igneous Systems. Reviews in Mineralogy and Geochemistry, 87(1), 607-638.

Nelson, S., and Montana, A. (1992) Sieve-textured plagioclase in volcanic rocks produced by rapid decompression. American Mineralogist, 77, 1242-1249.

Osborne, Z.R., Thomas, J.B., Nachlas, W.O., Angel, R.J., Hoff, C.M., and Watson, E.B. (2022) TitaniQ revisited: expanded and improved Ti-in-quartz solubility model for thermobarometry. Contributions to Mineralogy and Petrology, 177(3).

Pichavant, M., Costa, F., Burgisser, A., Scaillet, B., Martel, C., and Poussineau, S. (2007) Equilibration Scales in Silicic to Intermediate Magmas Implications for Experimental Studies. Journal of Petrology, 48(10), 1955-1972.

Pizarro, C., Parada, M.A., Contreras, C., and Morgado, E. (2019) Cryptic magma recharge associated with the most voluminous 20th century eruptions (1921, 1948 and 1971) at Villarrica Volcano. Journal of Volcanology and Geothermal Research, 384, 48-63.

Prouteau, G. (2003) Experimental Constraints on the Origin of the 1991 Pinatubo Dacite. Journal of Petrology, 44(12), 2203-2241.

Putirka, K.D. (2008) Thermometers and Barometers for Volcanic Systems. Reviews in Mineralogy and Geochemistry, 69(1), 61-120.

Qin, X.F., Wang, Z.Q., Zhang, Y.L., Pan, L.Z., Hu, G.A., and Zhou, F.S. (2011) Geochronology and geochemistry of Early Mesozoic acid volcanic rocks from Southwest Guangxi: Constraints on tectonic evolution of the southwestern segment of Qinzhou-Hangzhou joint belt. Acta Petrologica Sinica, 27(3), 794-808.

Ruprecht, P., Bergantz, G.W., Cooper, K.M., and Hildreth, W. (2012) The Crustal Magma Storage System of Volcán Quizapu, Chile, and the Effects of Magma Mixing on Magma Diversity. Journal of Petrology, 53(4), 801-840.

DOI: https://doi.org/10.2138/am-2022-8642. http://www.minsocam.org/

Schaen, A.J., Singer, B.S., Cottle, J.M., Garibaldi, N., Schoene, B., Satkoski, A.M., and Fournelle, J. (2018) Textural and Mineralogical Record of Low Pressure Melt Extraction and Silicic Cumulate Formation in the late Miocene Risco Bayo-Huemul Plutonic Complex, Southern Andes. Journal of Petrology.

Schiller, D., and Finger, F. (2019) Application of Ti-in-zircon thermometry to granite studies: problems and possible solutions. Contributions to Mineralogy and Petrology, 174(6), 51.

Shaw, S.E., and Flood, R.H. (2009) Zircon Hf Isotopic Evidence for Mixing of Crustal and Silicic Mantle-derived Magmas in a Zoned Granite Pluton, Eastern Australia. Journal of Petrology, 50(1), 147-168.

Singer, B.S., Costa, F., Herrin, J.S., Hildreth, W., and Fierstein, J. (2016) The timing of compositionally-zoned magma reservoirs and mafic ‘priming’ weeks before the 1912 Novarupta-Katmai rhyolite eruption. Earth and Planetary Science Letters, 451, 125-137.

Stevens, G., Villaros, A., and Moyen, J.-F. (2007) Selective peritectic garnet entrainment as the origin of geochemical diversity in S-type granites. Geology, 35(1).

Stewart, A.L., and McPhie, J. (2003) Internal structure and emplacement of an Upper Pliocene dacite cryptodome, Milos Island, Greece. Journal of Volcanology and Geothermal Research, 124(1-2), 129-148.

Student, J., J., and Bodnar, R.J. (1999) Synthetic Fluid Inclusions XIV: Coexisting Silicate Melt and Aqueous Fluid Inclusions in the Haplogranite–H_2O–NaCl–KCl System. Journal of Petrology, 40(10), 1509–1525.

Student, J.J., and Bodnar, R.J. (2004) Silicate melt inclusions in porphyry copper deposit. The Canadian Mineralogist, 42, 1583-1599

Taisne, B., and Jaupart, C. (2011) Magma expansion and fragmentation in a propagating dyke. Earth and Planetary Science Letters, 301(1-2), 146-152.

Tavazzani, L., Peres, S., Sinigoi, S., Demarchi, G., Economos, R.C., and Quick, J.E. (2020) Timescales and Mechanisms of Crystal-mush Rejuvenation and Melt Extraction Recorded in Permian Plutonic and Volcanic Rocks of the Sesia Magmatic System (Southern Alps, Italy). Journal of Petrology, 61(5).

Thomas, J.B., Bruce Watson, E., Spear, F.S., Shemella, P.T., Nayak, S.K., and Lanzirotti, A. (2010) TitaniQ under pressure: the effect of pressure and temperature on the solubility of Ti in quartz. Contributions to Mineralogy and Petrology, 160(5), 743-759.

Troch, J., Ellis, B.S., Harris, C., Bachmann, O., and Bindeman, I.N. (2020) Low-δ^{18}O silicic magmas on Earth: A review. Earth-Science Reviews, 208.

Wark, D.A., Hildreth, W., Spear, F.S., Cherniak, D.J., and Watson, E.B. (2007) Pre-eruption recharge of the Bishop magma system. Geology, 35(3).

Warren, I., Simmons, S.F., and Mauk, J.L. (2007) Whole-Rock Geochemical Techniques for Evaluating Hydrothermal Alteration, Mass Changes, and Compositional Gradients Associated with Epithermal Au-Ag Mineralization. Economic Geology, 102, 923–948.

Watt, G.R., Wright, P., Galloway, S., and McLean, C. (1997) Cathodoluminescence and trace element zoning in quartz phenocrysts and xenocrysts. Geochemica Cosmochimica Acta, 61(20), 4337-4348.

Watts, K.E., John, D.A., Colgan, J.P., Henry, C.D., Bindeman, I.N., and Schmitt, A.K. (2016) Probing the Volcanic–Plutonic Connection and the Genesis of Crystal-rich Rhyolite in a Deeply Dissected Supervolcano in the Nevada Great Basin: Source of the Late Eocene Caetano Tuff. Journal of Petrology, 57(8), 1599-1644.

Whitney, D.L., and Evans, B.W. (2009) Abbreviations for names of rock-forming minerals. American Mineralogist, 95(1), 185-187.

Wu, L.G., Li, Y., Jollands, M.C., Vermeesch, P., and Li, X.H. (2022) Diffuser: A user-friendly program for diffusion chronometry with robust uncertainty estimation. Computers & Geosciences, 163.

Wu, T., Zhou, J.-X., Wang, X.-C., Li, W.-X., Wilde, S.A., Sun, H.-R., Wang, J.-S., and Li, Z. (2018) Identification of ca. 850 Ma high-temperature strongly peraluminous granitoids in southeastern Guizhou Province, South China: A result of early extension along the southern margin of the Yangtze Block. Precambrian Research, 308, 18-34.

Xu, X., Zhao, K., He, Z., Liu, L., and Hong, W. (2021) Cretaceous volcanic-plutonic magmatism in SE China and a genetic model. Lithos, 402-403, 105728.

Yan, L., He, Z., Beier, C., and Klemd, R. (2018) Geochemical constraints on the link between volcanism and plutonism at the Yunshan caldera complex, SE China. Contributions to Mineralogy and Petrology, 173(1).

Yan, L.L., He, Z.-Y., Jahn, B.M., and Zhao, Z.D. (2016) Formation of the Yandangshan volcanic–plutonic complex (SE China) by melt extraction and crystal accumulation. Lithos, 266-267, 287-308.

Yan, L.L., He, Z.-Y., Klemd, R., Beier, C., and Xu, X.S. (2020) Tracking crystal-melt segregation and magma recharge using zircon trace element data. Chemical Geology, 542.

Yang, L.Z., Liu, R.T., and Bai, Y.P. (2011) The Early-Middle Triassic volcanic event-the Taima porphyroclastic lava in the Qinzhou area, southern Guangxi, China. Geological Bulletin of China, 30(1), 95-100.

Zellmer, G. F., Edmonds, M. and Straub, S. M. (2015) Volatiles in subduction zone magmatism. In: Zellmer, G. F., Edmonds, M. & Straub, S. M. (eds) The Role of Volatiles in the Genesis, Evolution and Eruption of Arc Magmas.

Zhang, C., Li, X., Almeev, R.R., Horn, I., Behrens, H., and Holtz, F. (2020) Ti-in-quartz thermobarometry and TiO_2 solubility in rhyolitic melts: New experiments and parametrization. Earth and Planetary Science Letters, 538.

Zhao, K., Xu, X., and Erdmann, S. (2017a) Crystallization conditions of peraluminous charnockites: constraints from mineral thermometry and thermodynamic modelling. Contributions to Mineralogy and Petrology, 172(5).

Zhao, K., Xu, X., and Erdmann, S. (2018) Thermodynamic modeling for an incrementally fractionated granite magma system: Implications for the origin of igneous charnockite. Earth and Planetary Science Letters, 499, 230-242.

Zhao, K., Xu, X., Erdmann, S., Liu, L., and Xia, Y. (2017b) Rapid migration of a magma source from mid- to deep-crustal levels: Insights from restitic granulite enclaves and anatectic granite. GSA Bulletin, 129, 1708–1725.

Zhou, X.M., Sun, T., Shen, W.Z., Shu, L.S., and Niu, Y. (2006) Petrogenesis of Mesozoic granitoids and volcanic rocks in South China: A response to tectonic evolution. Episodes, 29(1), 26-33.

Zieg, M.J., and Marsh, B.D. (2012) Multiple Reinjections and Crystal-mush Compaction in the Beacon Sill, McMurdo Dry Valleys, Antarctica. Journal of Petrology, 53(12), 2567-2591.

Figure captions

Figure 1. (a) Tectonic schematic map of South China and its surrounding plates (modified after Zhao et al. 2017b and references therein). Square refers to the location of the Qinzhou Bay

Granitic Complex. (b) Geological map showing the Qinzhou Bay Granitic Complex (QBGC). Stars mark our sample locations. (c) Geological profile showing that the locally extruded Taima porphyritic magma overlies the tuff layers of the Banba Formation (modified from Yang et al. 2011).

Figure 2. Microphotographs of the Banba rhyolite. (a) Optical microscope image showing millimeter-scale quartz (Qz) and plagioclase (Pl) phenocrysts with round and/or embayed outlines; (b) Backscattered electron (BSE) image showing sieve-like quartz phenocrysts and fine groundmass with elongated, dendritic quartz (black color); (c, d) Cathodoluminescence (CL) images showing unzoned and inversely zoned quartz phenocrysts; (e) Optical microscope image showing a group of melt inclusions (5-14 μm diameter) after homogenization; (f) Micro X-ray fluorescence (XRF) image of the thin section showing the distributions of Al and Fe elements, which are mostly enriched in cordierite (green, Crd); arrows denote the partially well-developed crystal faces. Mineral abbreviations after Whitney and Evans (2010).

Figure 3. (a) Columnar jointing developed in the Taima porphyritic cryptodome; (b) Groundmass of the Taima porphyry showing quartz crystals (dark color) with subhedral forms with partially developed hexagonal crystal faces; (c, d) Mineral phase mapping showing the mineral assemblage and texture of the Taima (a) and Dasi (b) porphyries; (e, f) Cathodoluminescence images showing quartz phenocrysts with dark cores and brighter overgrowths.

Figure 4. Quartz trace element contents of Al (a) and Fe (b) varying with widely variable Ti contents for the Banba rhyolite (green circles), Taima (orange diamonds) and Dasi (blue squares) porphyries, early Jiuzhou monzogranite (white-filled red triangles), late Jiuzhou charnockite (red triangles), and gneiss/schist xenoliths (circles). Quartz crystals in the rhyolite and porphyry units are divided into Groups A, B and C based on the probability distributions of Ti contents (curves along the horizontal axis). (c) Different covariant trends (I and II) of quartz Fe and Al contents in the studied volcanic and plutonic units. The dashed curve embraces Group A quartz from the Banba rhyolite. Error bars show the average 2σ uncertainties.

Figure 5. Profiles of quartz Ti zoning for the Banba rhyolite (a) and the Taima porphyry (c). Ti contents are estimated based on CL intensities, as the CL intensity and measured Ti content of quartz crystals from the same epoxy mount have good correlations (b, d).

Figure 6. Anorthite content profiles of plagioclase phenocrysts in the Taima and Dasi porphyries. The white dashed lines with white boxes in the left panels denote the BSE-based profiles corresponding to black lines in the right panels. The BSE-based profiles are obtained from measurements of the accumulated BSE images using ImageJ software because the emission intensity of BSE depends mainly on the An contents (Ginibre et al. 2002), and each point of the profile represents the luminance averaged over a sampling area (3×5 pixels). The red lines in the left panels represent compositional profiles of EMP analyses corresponding to the red diamonds in the right panels. The thin dotted lines outline the resorption surfaces. Abbreviations: An, anorthite content; r, resorption surface; og, overgrowth.

Figure 7. Distributions of anorthite contents for plagioclase phenocryst cores (a) and overgrowths (b) and groundmass (c) in the Taima and Dasi porphyries.

Figure 8. Zircon trace element contents of Ti (a) and P (b) and values of Nb/Ta (c) and Zr/Hf (d) varying as a function of Eu/Eu* in the Banba rhyolite, Taima and Dasi porphyries, and Jiuzhou charnockite. Arrows denote the outliers determined by comparison with zircon saturation temperatures (see Fig. 11). Error bars show average 2σ uncertainties, and the error bar of the Zr/Hf ratio is smaller than the symbol size.

Figure 9. Harker diagrams showing the variations in Al_2O_3 (a), Fe_2O_3 (b), MgO (c), CaO (d), Na_2O (e) and K_2O (f) contents with variable SiO_2 contents for whole-rock, melt inclusion and groundmass compositions. The purple, green and blue dashed lines denote liquid evolution trends at 150 MPa, 100 MPa and 50 MPa modeled from the Rhyolite_MELTS software (v.1.1.x, Gualda et al. 2012a). The modeling employs the least evolved melt inclusion as the parental melt and is conducted with 2.5 wt% initial H_2O content (determined through volatiles by difference method using EPMA) and oxygen fugacity corresponding to the QFM buffer (Jiao et al. 2015). The whole-rock data of the late Jiuzhou granite (solid red triangles), the Taima and Dasi porphyries (solid orange diamonds and solid blue squares) and the Banba rhyolite (gray circles with green outlines) are from the literature (Qin et al. 2011; Jiao et al. 2016; Zhao et al. 2017b). The outlier (BB02-1) with high FeO and MgO contents for the Banba samples is likely caused by the involvement of xenolithic/xenocrystic materials during the deposit process (Fig. S1a) and thus is not taken into consideration. Error bars are indicated when larger than the symbol size.

This is the peer-reviewed, final accepted version for American Mineralogist, published by the Mineralogical Society of America.
The published version is subject to change. Cite as Authors (Year) Title. American Mineralogist, in press.
DOI: https://doi.org/10.2138/am-2022-8642. http://www.minsocam.org/

Figure 10. (a) Sr-Nd isotope compositions of the volcanic and plutonic rocks. Data of the Taima and Dasi porphyries and the late Jiuzhou pluton after Zhao et al. (2017b). Dashed green and blue lines with diamonds denote the variation trends of mixing with amphibole-bearing dacites: one endmember is represented by the adjacent Beisi dacites (with $^{143}Nd/^{144}Nd$ = 0.511859 and $^{87}Sr/^{86}Sr$ = 0.714425; Qin et al. 2011); another endmember is represented by sample JZ03-4 (see supplementary table S2). (b) Variation in whole-rock $\delta^{18}O$ values with SiO_2 contents. The histograms represent calculated whole-rock $\delta^{18}O$ values based on equilibrium fractionation with zircon oxygen isotopes (zircon data after Jiao et al. 2015; method following Lackey et al. 2008). Shaded fields represent the main range of the calculated whole-rock $\delta^{18}O$ values for the Banba rhyolite and the Taima and Dasi porphyries.

Figure 11. Crystallization temperature distributions of zircon at $aTiO_2$ of 0.5 (a) and 0.75 (b) for volcanic-plutonic units. The probability density curves along the horizontal axis denote the normal distributions of Ti-in-zircon temperatures. The grains enclosed by dashed lines represent potential antecrysts or inherited crystals, which have temperatures higher than zircon saturation temperatures (T_{sat}). The main temperature interval of zircon crystallization is represented by 2σ confidence level (e.g., 836±32 °C). Error bars mark the maximum standard error of the median temperature.

Figure 12. P–T phase relationship constrained by thermodynamic modeling (using Perple_X software; Connolly 2005) for the Banba rhyolite at 1.0 wt% (a), 1.5 wt% (b) and 2.0 wt% (c) initial melt H_2O contents. The modeling is conducted using the reconstructed compositions of reactive magma with ~72.3% SiO_2 (supplementary table S1). Colored lines mark the stability

fields of different phases, and gray dashed lines denote the crystallinity isopleths (in vol%). The gray thick dashed and black thin dashed lines represent the experimental solidus (from Holtz et al. 2001) and modeled solidus, respectively. Thermobarometric results are also marked in the figures for comparison: gray shadows and dashed rectangles indicate the range of Ti-in-zircon temperature at $aTiO_2$ of 0.5 and 0.75 (Fig. 11a, b); solid and white circles with thick lines denote the range of Ti-in-quartz temperature at corresponding pressure at $aTiO_2$ of 0.5 and 0.75 (Fig. 14a, b).

Figure 13. P–T phase relationship constrained by thermodynamic modeling (using Perple_X software; Connolly 2005) for the Taima porphyry at 1.5 wt% (a) and 2 wt% (b) initial melt H_2O contents. The modeling is conducted using the reconstructed compositions of reactive magma with ~71.0 wt% SiO_2 and ~1.3 wt% CaO (supplementary table S1). See the caption of Fig. 9 for the legend. (c) The modeled anorthite contents of plagioclase varying as a function of temperature at 150 MPa and different initial melt H_2O contents.

Figure 14. Thermobarometric results from Ti content in quartz shown in a P–T space at $aTiO_2$ of 0.5 and 0.75 (after Zhang et al. 2020). Colored circles with thick lines denote the P–T crystallization conditions of different groups of quartz (Fig. 4). The orange and blue circles with black outlines represent the P–T conditions of bright overgrowth of quartz in the Taima and Dasi porphyries (with 330-350 ppm Ti inferred from CL intensity; Fig. 3c, d).

Figure 15. (a) Molar element ratio plot of K/Al versus (2Ca + Na + K)/Al for the peraluminous volcanic and plutonic rocks. Gray circles with green outlines denote the whole-rock data of the

Banba rhyolitic lavas from the literature (Qin et al. 2011; Jiao et al. 2016). (b-f) Harker diagram showing how the proposed magmatic processes influence the compositional variation of the Banba rhyolites. Green solid lines represent the fractionation trends of Banba melts, which are defined by compositions of cumulates (black-outlined circles labeled with fractions of extracted melts, i.e., 10-40%) and fractionated melts (green-outlined circles labeled with fractions of unsegregated phenocrysts, i.e., 10-30%). Green points denote the parental magma represented by the least evolved melt inclusion. The combined effects of magma recharge and fractionation are shown by the black solid and green dashed lines.

Figure 16. Schematic cartoons illustrating the temporal evolution of the studied magma systems. The sequentially developed volcanic-plutonic units experienced complex magmatic processes with temporal evolution. (a) Hybridization between metasediment-sourced magmas and dacitic magmas generated Cl-rich, metaluminous magmas in the middle crust; Crystal-liquid segregation produced crystal-poor evolved magmas in the upper crust; Recharge and mixing occurred in a shallow reservoir where Group A quartz crystallized. (b) Recharge of new metasediment-sourced magmas caused reactivation and convection of the mushy zone, leading to magma ascent and emplacement at ultrashallow levels. (c) At a waning stage, the late Jiuzhou magmas were derived from melting of the metasedimentary source and intruded into the unerupted part of the reservoir (i.e., the early Jiuzhou pluton).

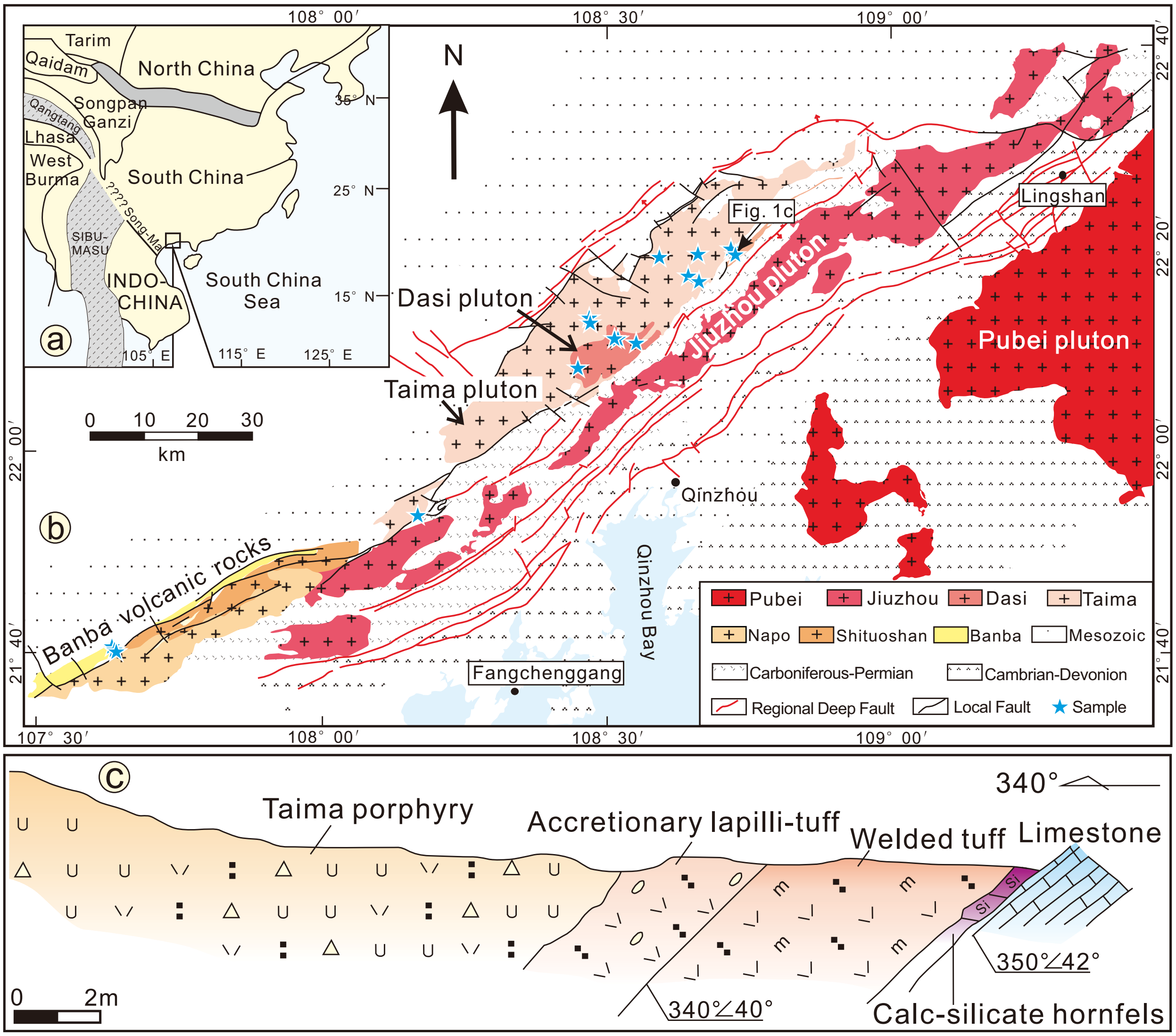
Tarim
Qaidam
North China
Songpan Ganzi
Qangtang
Lhasa
West Burma
South China
SIBU-MASU
Song-Ma
INDO-CHINA
South China Sea
35° N
25° N
15° N
105° E
115° E
125° E
a
b
c
N
108° 00′
108° 30′
109° 00′
107° 30′
22° 40′
22° 20′
22° 00′
21° 40′
0 10 20 30
km
Fig. 1c
Lingshan
Dasi pluton
Jiuzhou pluton
Pubei pluton
Taima pluton
Qinzhou
Qinzhou Bay
Banba volcanic rocks
Fangchenggang
Pubei
Jiuzhou
Dasi
Taima
Napo
Shituoshan
Banba
Mesozoic
Carboniferous-Permian
Cambrian-Devonion
Regional Deep Fault
Local Fault
Sample
340°
Taima porphyry
Accretionary lapilli-tuff
Welded tuff
Limestone
Si
350°∠42°
340°∠40°
Calc-silicate hornfels
0 2m

Figure 1

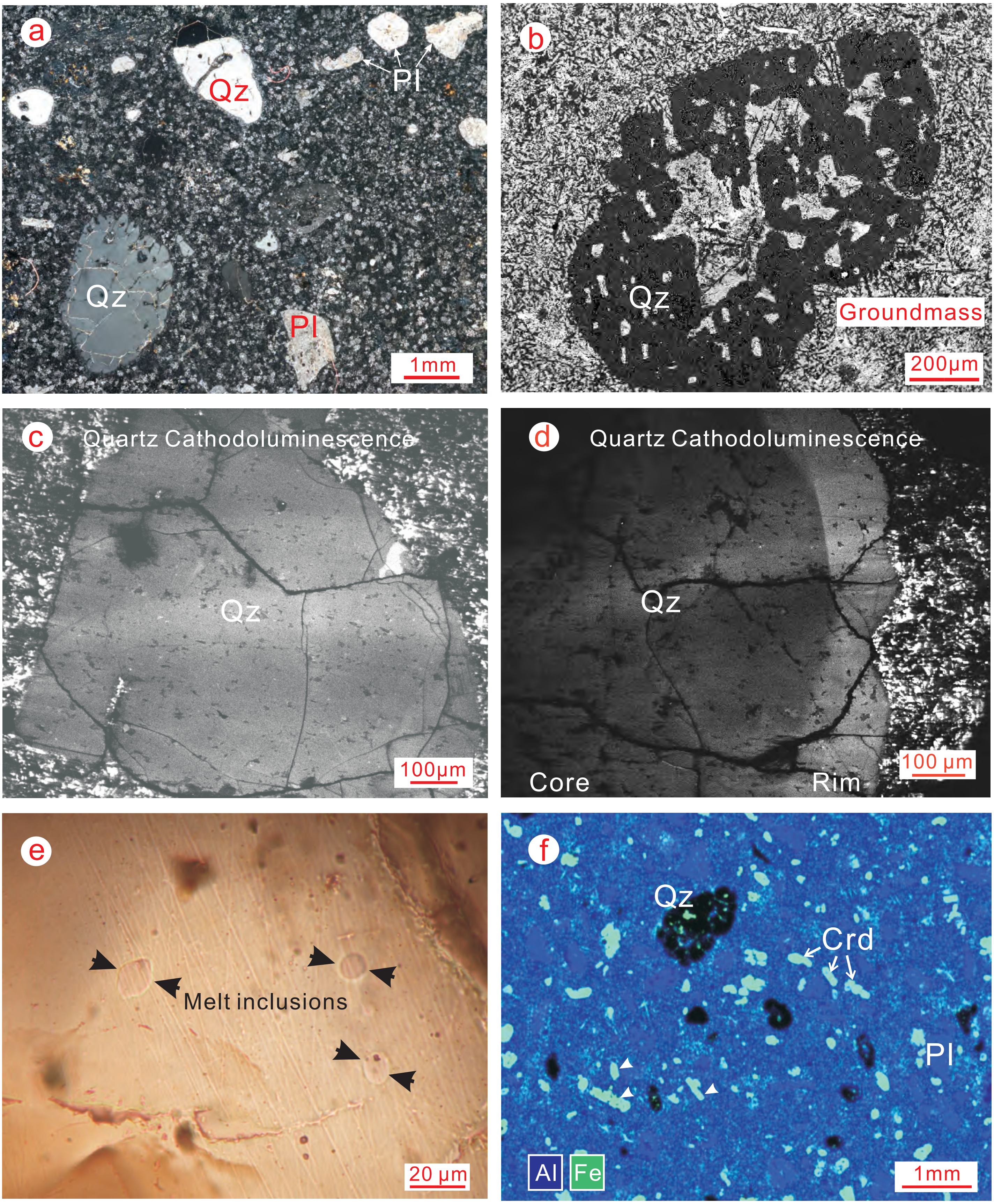
a
Qz
Pl
Qz
Pl
1mm
b
Qz
Groundmass
200μm
c
Quartz Cathodoluminescence
Qz
100μm
d
Quartz Cathodoluminescence
Qz
Core
Rim
100 μm
e
Melt inclusions
20 μm
f
Qz
Crd
Pl
Al
Fe
1mm

Figure 2

This is the peer-reviewed, final accepted version for American Mineralogist, published by the Mineralogical Society of America.
The published version is subject to change. Cite as Authors (Year) Title. American Mineralogist, in press.
DOI: https://doi.org/10.2138/am-2022-8642. http://www.minsocam.org/

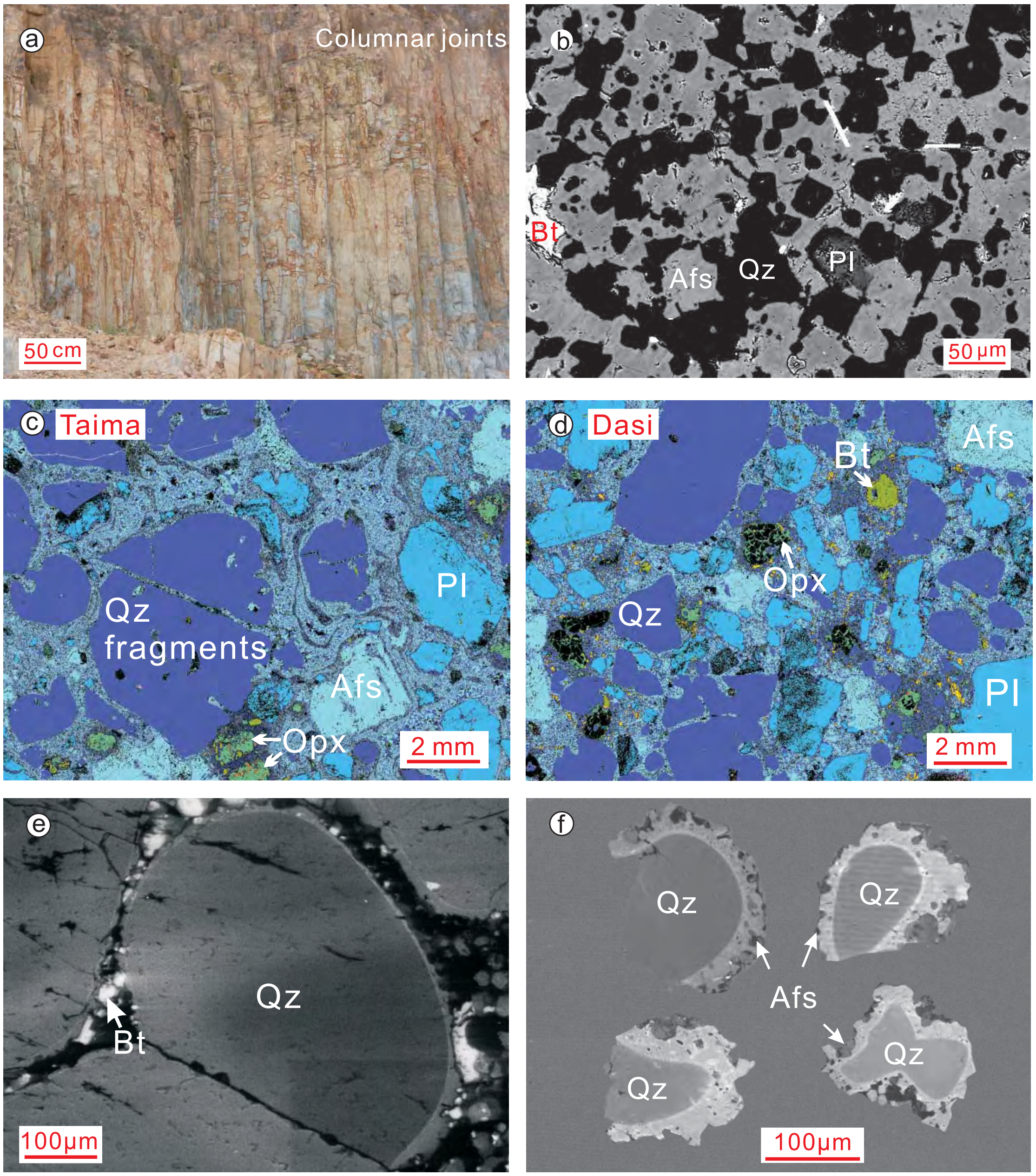

Figure 3

This is the peer-reviewed, final accepted version for American Mineralogist, published by the Mineralogical Society of America.
The published version is subject to change. Cite as Authors (Year) Title. American Mineralogist, in press.
DOI: https://doi.org/10.2138/am-2022-8642. http://www.minsocam.org/

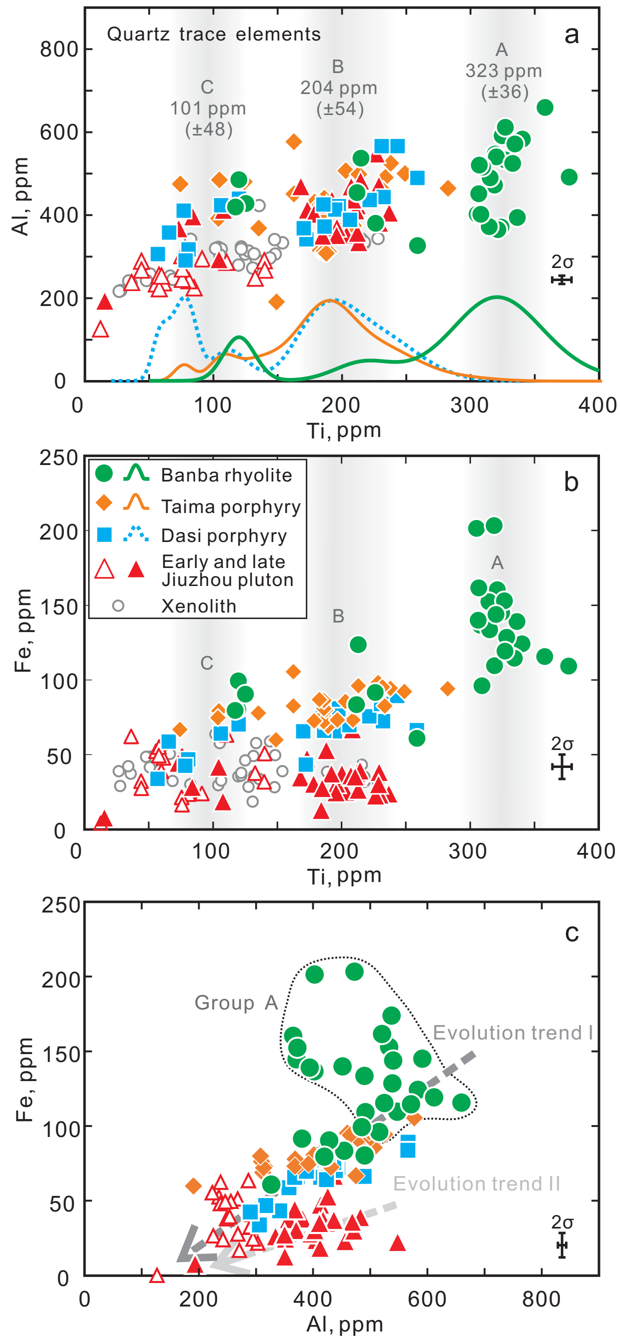

Figure 4

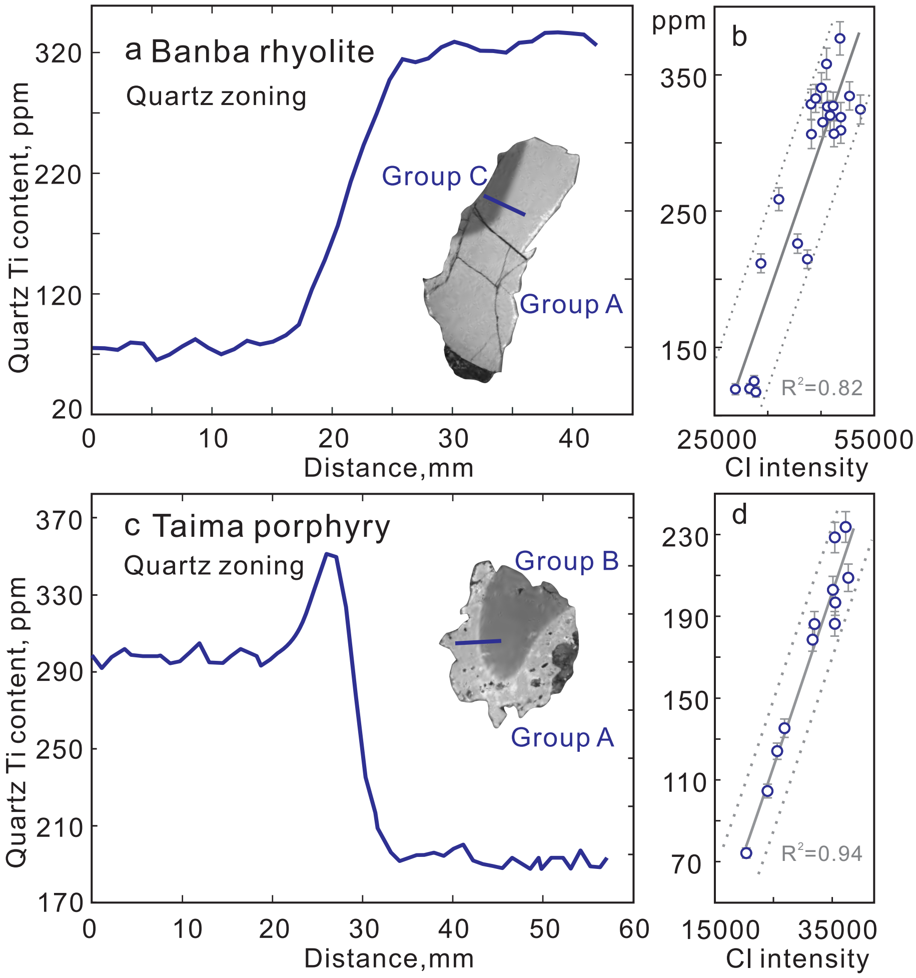
a Banba rhyolite
Quartz zoning
Group C
Group A
Quartz Ti content, ppm
320
220
120
20
0
10
20
30
40
Distance,mm
ppm
b
350
250
150
R²=0.82
25000
55000
CI intensity
c Taima porphyry
Quartz zoning
Group B
Group A
370
330
290
250
210
170
0
10
20
30
40
50
60
d
230
190
150
110
70
R²=0.94
15000
35000

Figure 5

This is the peer-reviewed, final accepted version for American Mineralogist, published by the Mineralogical Society of America.
The published version is subject to change. Cite as Authors (Year) Title. American Mineralogist, in press.
DOI: https://doi.org/10.2138/am-2022-8642. http://www.minsocam.org/

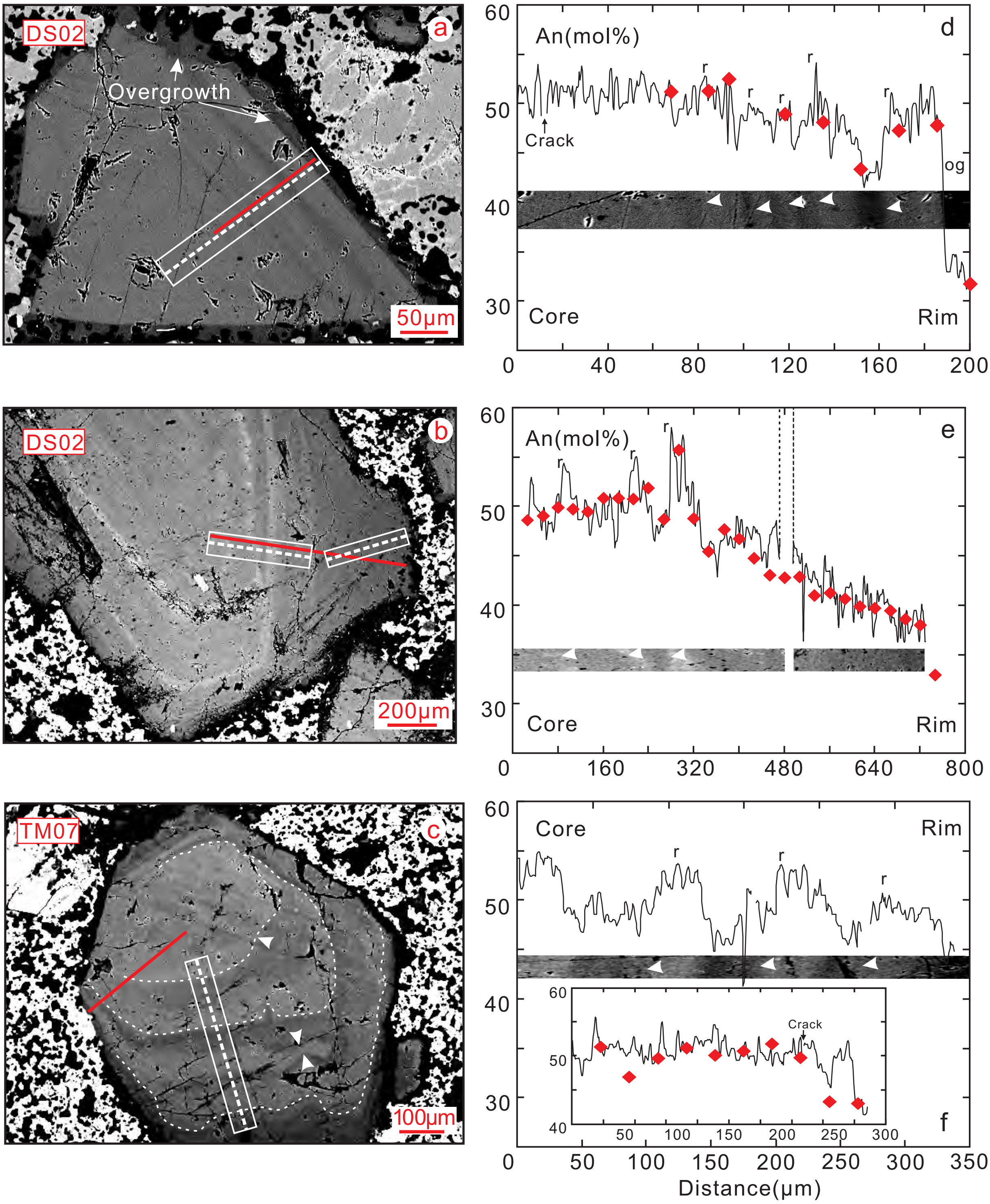

Figure 6

DOI: https://doi.org/10.2138/am-2022-8642. http://www.minsocam.org/

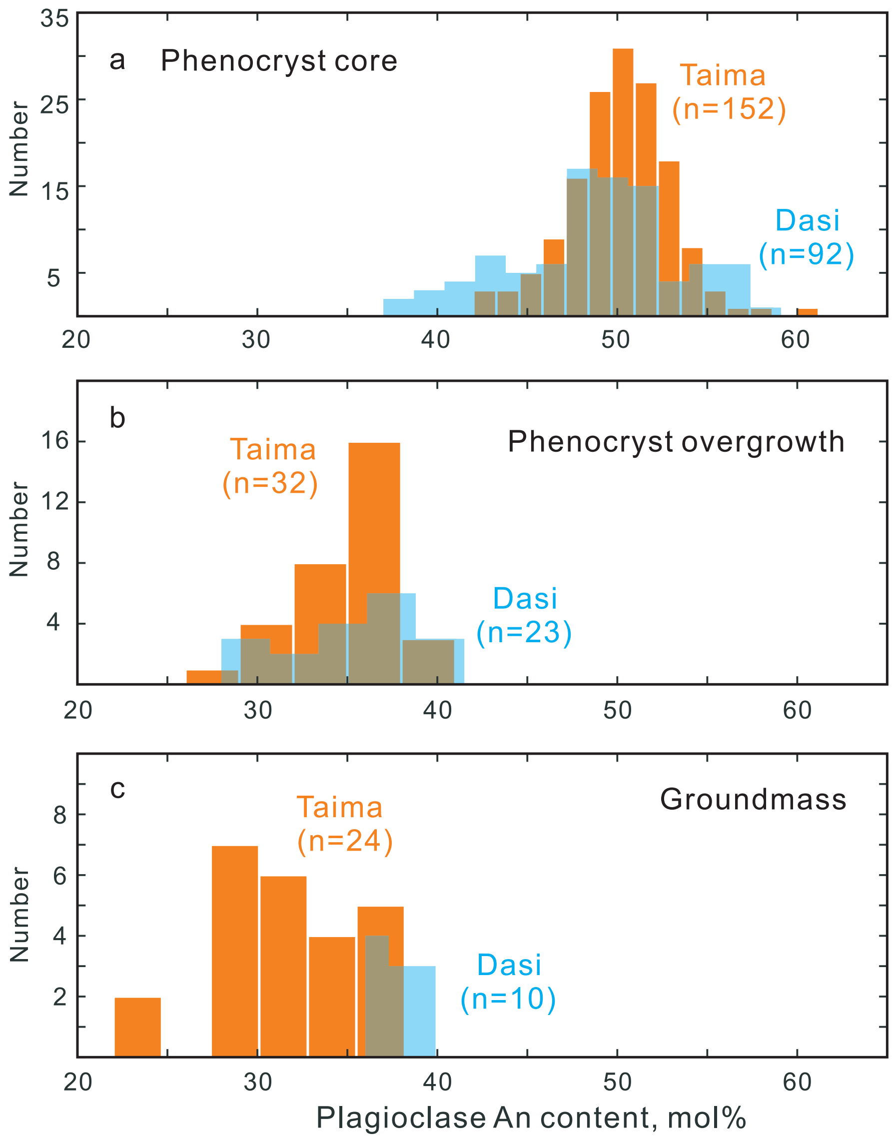

Figure 7

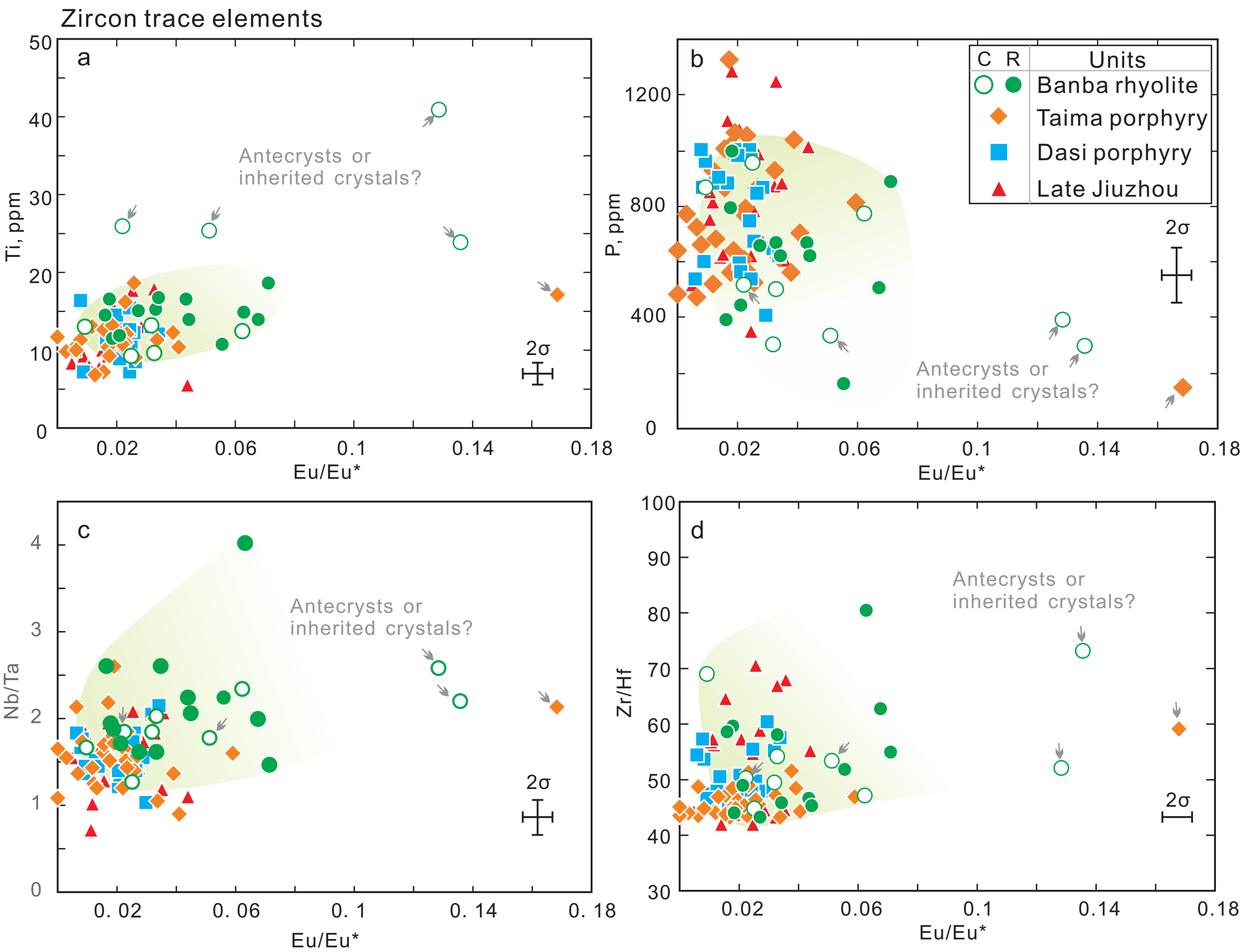
Zircon trace elements
a
Ti, ppm
Antecrysts or inherited crystals?
2σ
Eu/Eu*
b
P, ppm
C R Units
Banba rhyolite
Taima porphyry
Dasi porphyry
Late Jiuzhou
2σ
Antecrysts or inherited crystals?
Eu/Eu*
c
Nb/Ta
Antecrysts or inherited crystals?
2σ
Eu/Eu*
d
Zr/Hf
Antecrysts or inherited crystals?
2σ
Eu/Eu*

Figure 8

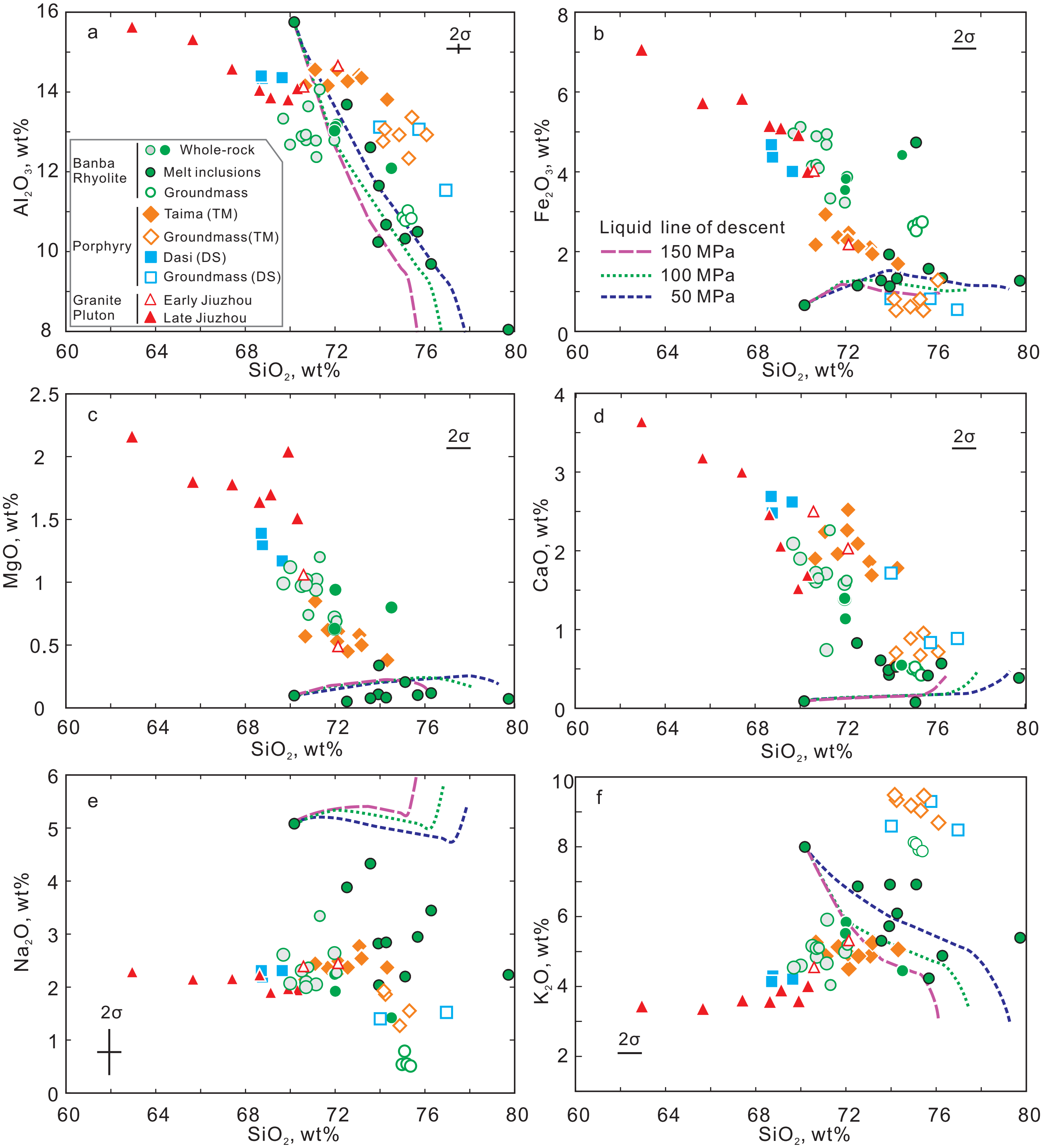
a
b
c
d
e
f
2σ
Al_2O_3, wt%
Fe_2O_3, wt%
MgO, wt%
CaO, wt%
Na_2O, wt%
K_2O, wt%
SiO_2, wt%
Banba Rhyolite
Whole-rock
Melt inclusions
Groundmass
Porphyry
Taima (TM)
Groundmass(TM)
Dasi (DS)
Groundmass (DS)
Granite Pluton
Early Jiuzhou
Late Jiuzhou
Liquid line of descent
150 MPa
100 MPa
50 MPa

Figure 9

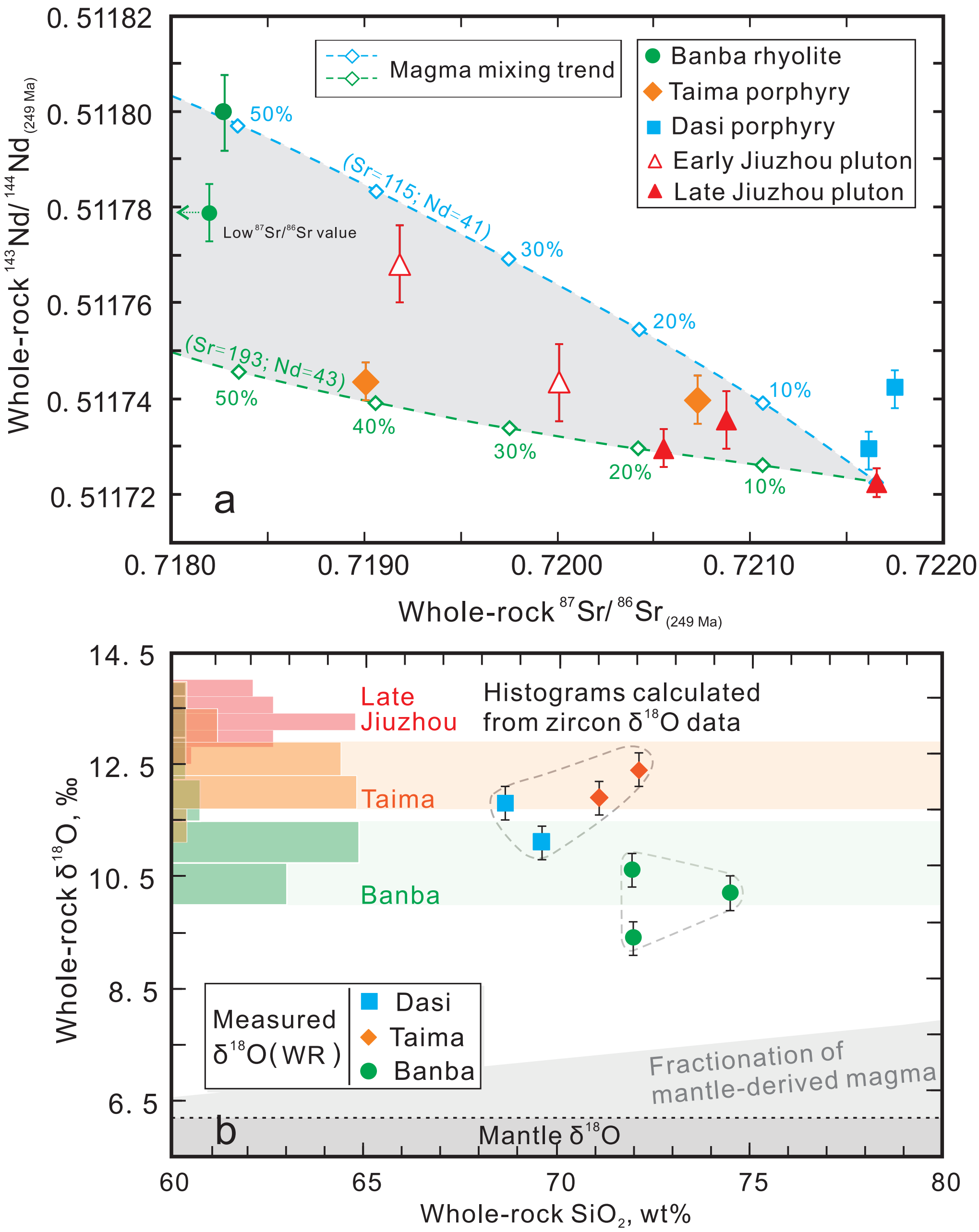
Magma mixing trend
Banba rhyolite
Taima porphyry
Dasi porphyry
Early Jiuzhou pluton
Late Jiuzhou pluton
(Sr=115; Nd=41)
(Sr=193; Nd=43)
50%
40%
30%
20%
10%
Low 87Sr/86Sr value
a
Whole-rock 143Nd/144Nd (249 Ma)
Whole-rock 87Sr/86Sr (249 Ma)
0. 51182
0. 51180
0. 51178
0. 51176
0. 51174
0. 51172
0. 7180
0. 7190
0. 7200
0. 7210
0. 7220
Late Jiuzhou
Histograms calculated from zircon δ18O data
Taima
Banba
Measured δ18O(WR)
Dasi
Taima
Banba
Fractionation of mantle-derived magma
Mantle δ18O
b
Whole-rock δ18O, ‰
Whole-rock SiO2, wt%
14. 5
12. 5
10. 5
8. 5
6. 5
60
65
70
75
80

Figure 10

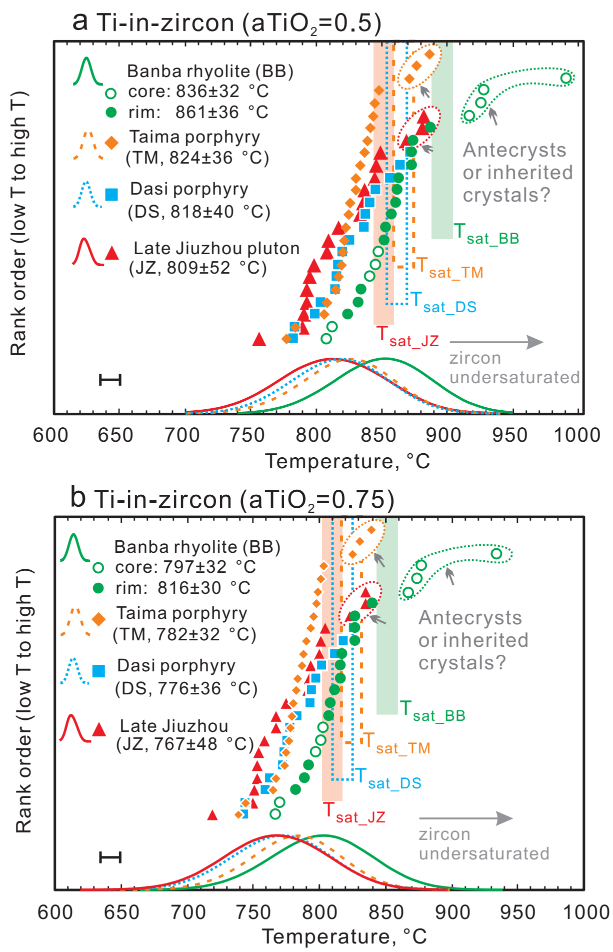
a Ti-in-zircon (aTiO2=0.5)
Banba rhyolite (BB)
core: 836±32 °C
rim: 861±36 °C
Taima porphyry
(TM, 824±36 °C)
Dasi porphyry
(DS, 818±40 °C)
Late Jiuzhou pluton
(JZ, 809±52 °C)
Antecrysts
or inherited
crystals?
Tsat_BB
Tsat_TM
Tsat_DS
Tsat_JZ
zircon
undersaturated
Rank order (low T to high T)
600 650 700 750 800 850 900 950 1000
Temperature, °C
b Ti-in-zircon (aTiO2=0.75)
Banba rhyolite (BB)
core: 797±32 °C
rim: 816±30 °C
Taima porphyry
(TM, 782±32 °C)
Dasi porphyry
(DS, 776±36 °C)
Late Jiuzhou
(JZ, 767±48 °C)
Antecrysts
or inherited
crystals?
Tsat_BB
Tsat_TM
Tsat_DS
Tsat_JZ
zircon
undersaturated
Rank order (low T to high T)
600 650 700 750 800 850 900 950 1000
Temperature, °C

Figure 11

DOI: https://doi.org/10.2138/am-2022-8642. http://www.minsocam.org/

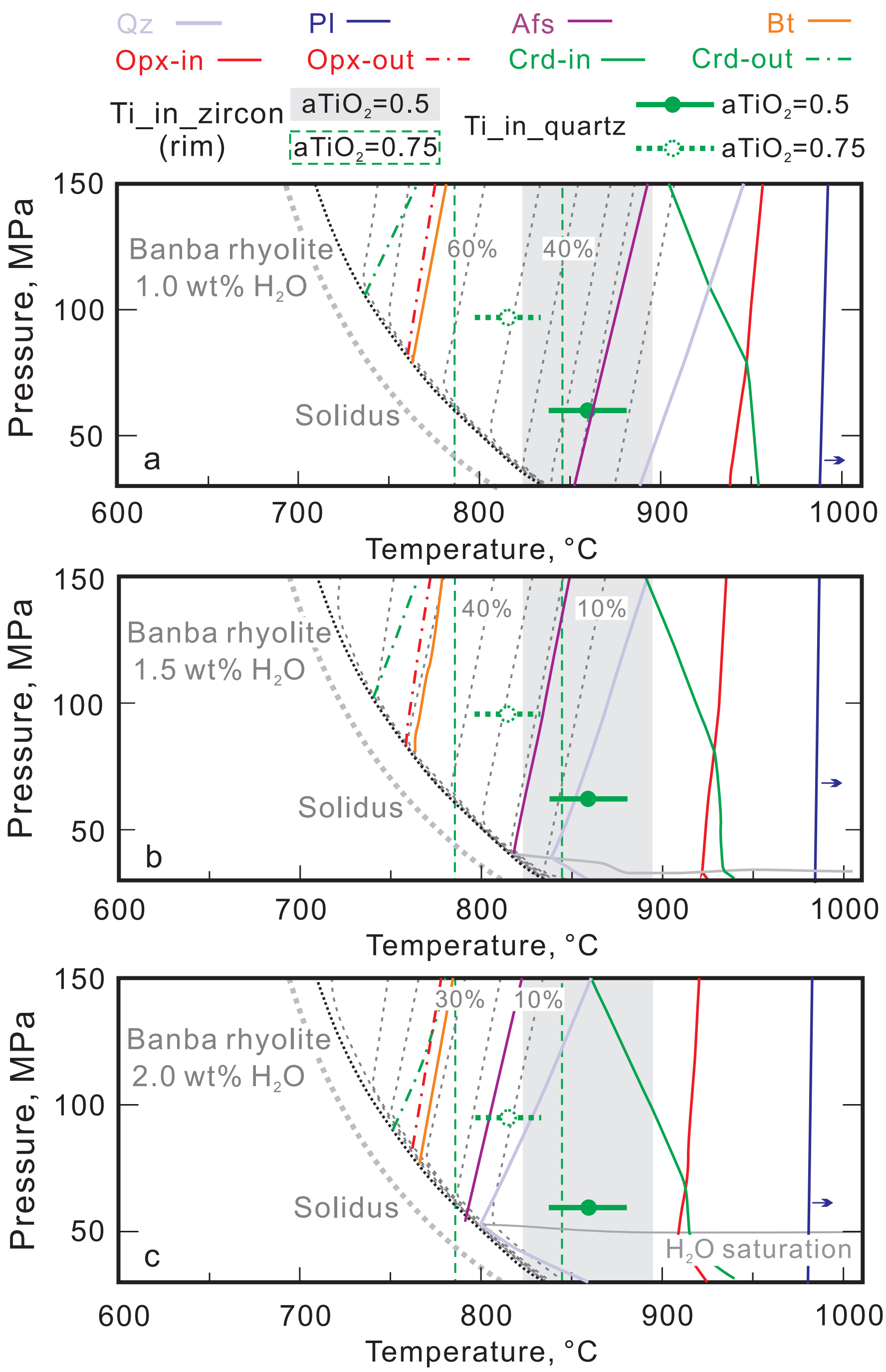

Figure 12

DOI: https://doi.org/10.2138/am-2022-8642. http://www.minsocam.org/

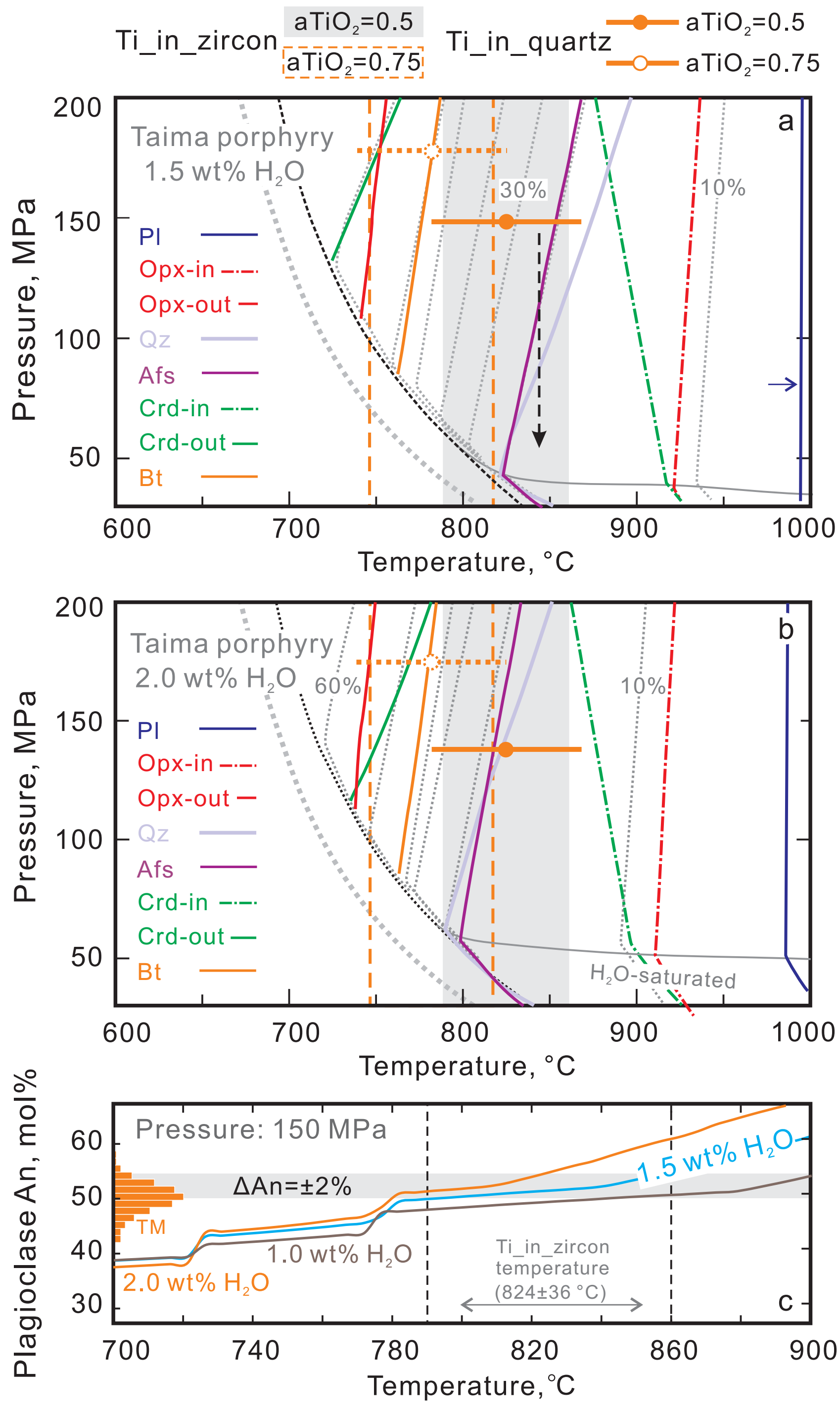

Figure 13

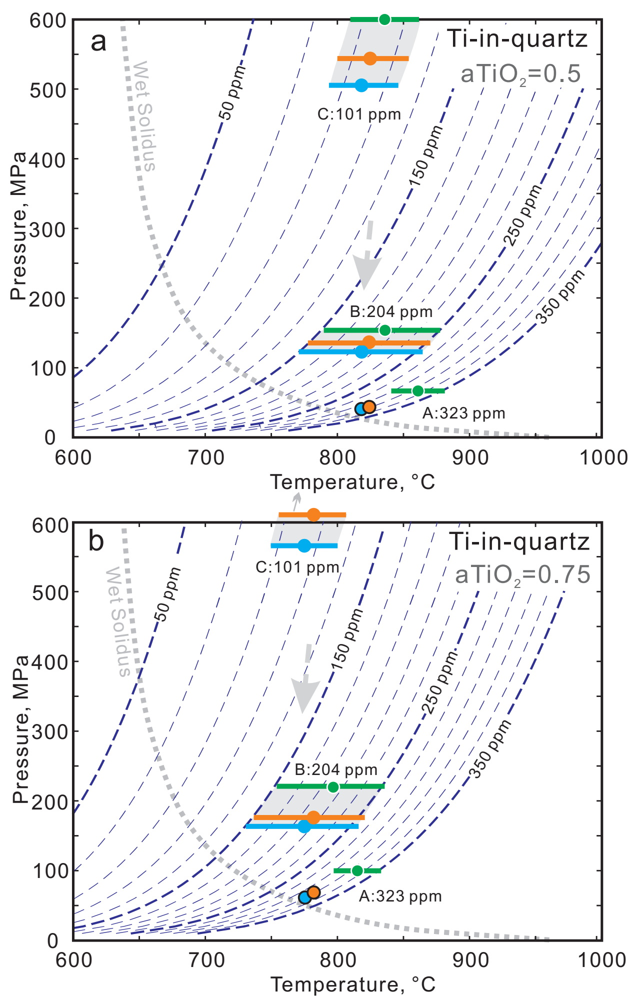
a
Ti-in-quartz
aTiO2=0.5
Wet Solidus
50 ppm
150 ppm
250 ppm
350 ppm
C:101 ppm
B:204 ppm
A:323 ppm
Pressure, MPa
Temperature, °C
b
Ti-in-quartz
aTiO2=0.75
Wet Solidus
50 ppm
150 ppm
250 ppm
350 ppm
C:101 ppm
B:204 ppm
A:323 ppm
Pressure, MPa
Temperature, °C

Figure 14

DOI: https://doi.org/10.2138/am-2022-8642. http://www.minsocam.org/

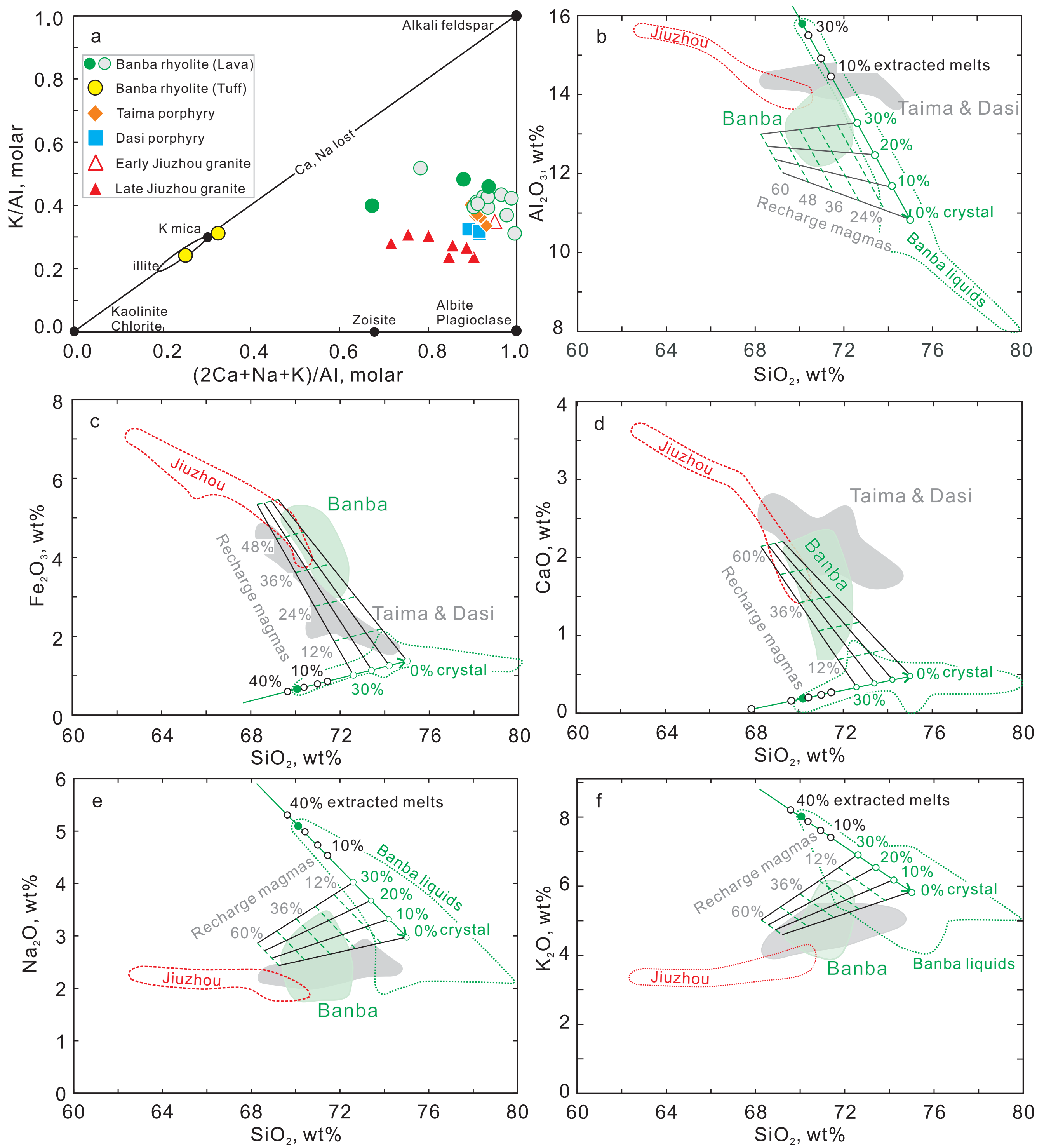

Figure 15

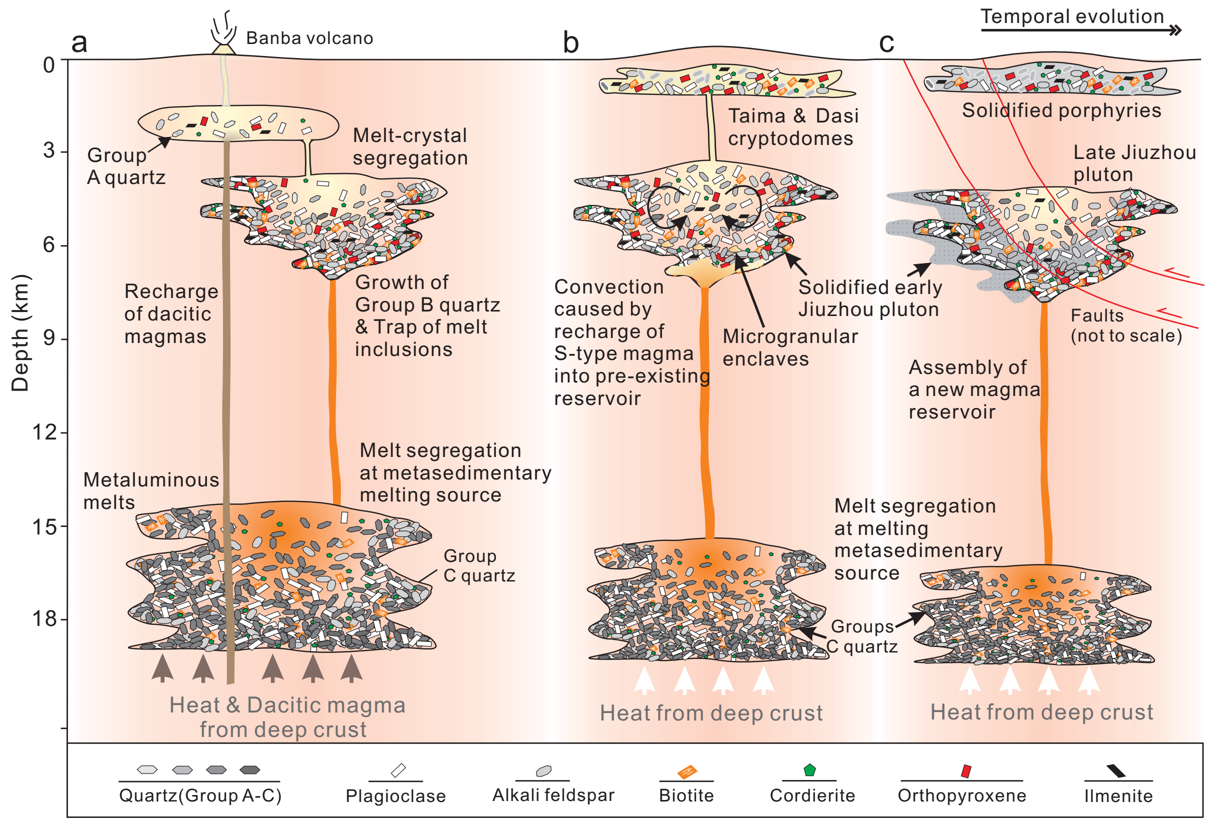
Temporal evolution
a
Banba volcano
b
c
0
3
6
9
12
15
18
Depth (km)
Group A quartz
Melt-crystal segregation
Recharge of dacitic magmas
Growth of Group B quartz & Trap of melt inclusions
Melt segregation at metasedimentary melting source
Metaluminous melts
Group C quartz
Heat & Dacitic magma from deep crust
Taima & Dasi cryptodomes
Convection caused by recharge of S-type magma into pre-existing reservoir
Solidified early Jiuzhou pluton
Microgranular enclaves
Heat from deep crust
Groups C quartz
Solidified porphyries
Late Jiuzhou pluton
Faults (not to scale)
Assembly of a new magma reservoir
Melt segregation at melting metasedimentary source
Quartz(Group A-C)
Plagioclase
Alkali feldspar
Biotite
Cordierite
Orthopyroxene
Ilmenite

Figure 16